UNIVERSITÀ DI TRENTO
Dipartimento di Fisica

NANOSCIENCE LABORATORY HIGHLIGHTS 2023

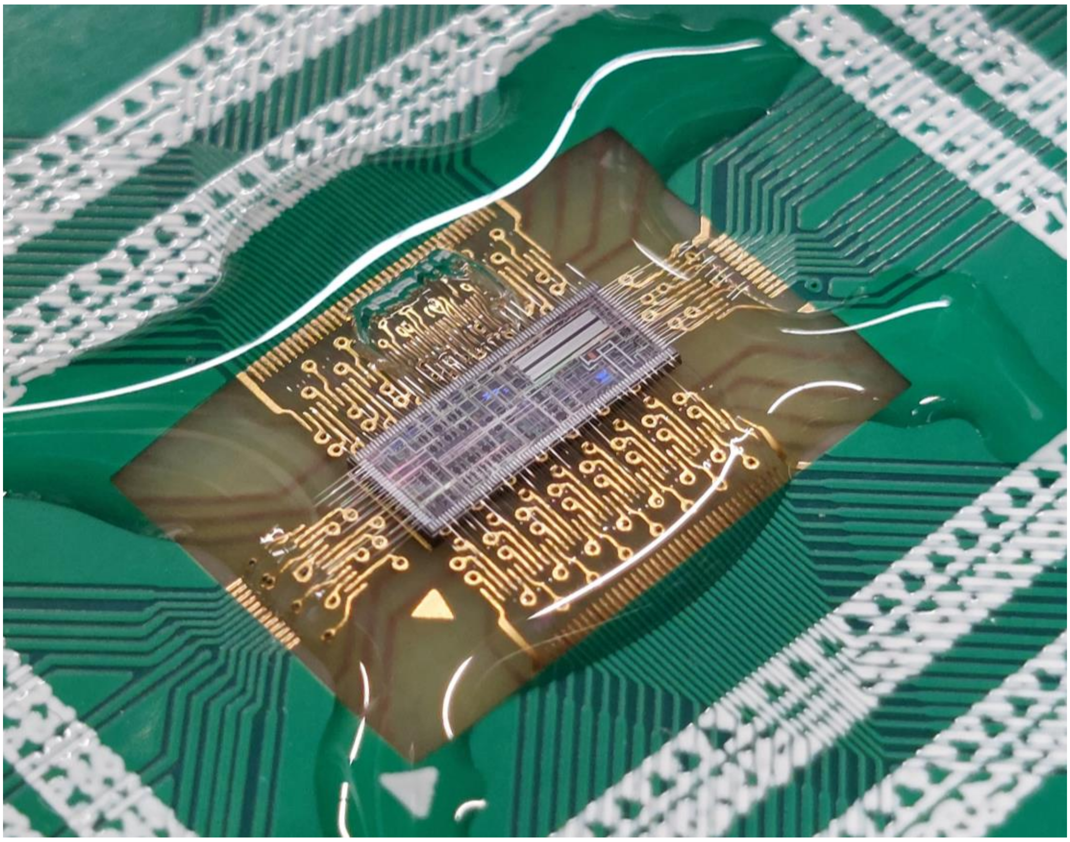

Image on the front cover: *A wirebonded photonic chip on a PCB and covered with an index matching glucose drop*
Photo by R. Franchi

NANOSCIENCE LABORATORY

MEMBERS (2023)

Faculty staff
Lorenzo Pavesi (full professor, head)
Marina Scarpa (full professor)
Zeno Gaburro (associate professor)
Paolo Bettotti (associate professor)
Stefano Azzini (associate professor)
Stefano Biasi (researcher)
Mattia Mancinelli (researcher, left January 2023)
Beatrice Vignoli (researcher)

Technical staff
Enrico Moser (left April 2023)
Elvira D'Amato

Post-docs
Bülent Aslan
Ilya Auslender
Alessio Baldazzi
Riccardo Franchi
Nicolò Leone
Alessio Lugnan
Clara Zaccaria

Administrative staff
Chiara Rindone
Camilla Kandamulla Arachchige

Doctoral students
Salamat Ali
Paolo Brunelli
Alessandro Foradori
Giovanni Donati (left July 2023)
Gianpietro Maddinelli
Asiye Malkoç
Chiara Michelini
Matteo Sanna
Emiliano Staffoli
Seyedeh Yasaman Heydari
Gianmarco Zanardi

Master students
Sara Bombardelli
Nicolò Broseghini
Leonardo Cattarin
Davide Micheli
Arianna Bartolomei

SCIENTIFIC MISSION

Introduction to the Nanoscience Laboratory

The Nanoscience Laboratory (NL) is one of the scientific groups of the Department of Physics, University of Trento. Its main areas of research are neuromorphic photonics, integrated quantum photonics, non-hermitian photonics and nanobiotechnologies. The mission of NL is to generate new knowledge, to develop understanding and to spin-off applications from physical phenomena associated with photons and their interactions with matter, particularly when it is nanostructured. Specifically, NL aims at understanding the optical and physical properties of ligthwave systems such as optical waveguides, microresonators and complex dielectric systems. NL covers the whole value chain from fundamental phenomena to device applications, where the photonic platform is compatible with the main driving silicon microelectronic technologies. In addition, quantum phenomena are studied as a resource for quantum information applications. Recently most of the activity has focused on the understanding and developing of novel computational paradigm both in the quantum realm as well as in the biological counterpart.
Another research theme at NL focuses on the exploitation of cellulose-derived materials. Both fundamental as well as applied studies are conducted to understand the properties and to fabricate devices using this fascinating natural biopolymer.

NL research group consists of more than 20 people with different scientific backgrounds. Researchers from physics, physiology, bio-chemistry, materials science and electrical engineering are gathered to form a group of interdisciplinary nature. It is worth mentioning that NL collaborates closely with the Center of Materials and Microsystems, Fondazione Bruno Kessler (FBK). This collaboration spans over the last thirty years and covers various topics such as fabrication, testing and application of biomaterials and silicon based devices. Both participate in many common projects. The current one is project EPIQUS. A strategic collaboration is ongoing with the Trento units of CNR-INO, specifically dedicated to implement quantum optics in integrated silicon chip. Finally, the activity on quantum information is within Q@TN, the joint laboratory between the University, FBK, CNR and INFN.
Moreover, with the support of FBK and CNR and every odd year, NL organizes a winter school on optoelectronics and photonics. The 12th edition was "PQIP 2023 – Photonic

Quantum Information Processing" in early 2023.
The research activities of NL are mainly supported by the local government (PAT), by the European Commission, by the Italian Ministry of Education, University and Research (MIUR) and by companies. During the period covered by these Highlights, NL has been involved in the following projects: PRIN-MIUR PELM "Photonics Extreme Learning Machine: from neuromorphic computing to universal optical interpolant, strain gauge sensor and cancer morphodynamic monitor"; PRIN-MIUR PANACEA "A technology PlAtform for the sustainable recovery and advanced use of NAnostructured CEllulose from Agri-food residues"; ERC-2017-ADG-788793 BACKUP: "Unveiling the relationship between brain connectivity and function by integrated photonics"; H2020-FETOPEN-01-2018-2019-2020 EPIQUS Electronic-photonic integrated quantum simulator platform; Q@TN project "Quantum Science and Technology in Trento".

Silicon Nanophotonics

Silicon photonics is the technology where photonic devices are produced by standard microelectronic processes using the same paradigm of electronics: integration of a large number of devices to yield a high circuit complexity, which allows for high performances and low costs. Here, the truth is to develop photonic devices that can be easily integrated to improve the single device performance and to allow high volume production.
We are mostly concentrated on two alternative approaches where photonics is used to compute. On one side we develop new scheme to implement artificial intelligent in a photonic silicon chip by using brain-inspired or neuromorphic computing schemes. On the other side, we use silicon photonics to provide a suitable platform for quantum computing and quantum simulations. In both approaches, one fundamental device is the silicon microresonator where whispering gallery modes induce nonlinearities, which can be exploited to generate new quantum states of light or to realize recurrent neural network. In addition, we use micro-disks or micro-rings to study new physics (chirality, exceptional points, entangled photon generation). The microresonators are coupled directly with narrow mode SOI (Silicon-on-Insulator) waveguides. Also, multimode waveguides are used for nonlinear frequency conversion or generation. Quantum science is used to develop novel imaging methodology which exploits entangled photons.
Lastly, hybrid chips are developed to interface living neurons with photonic waveguides in the search for artificial intelligence. Here, the signal transduction is achieved by using photo-sensitive proteins.

Advanced nanomaterials for energy, environment and life

In this research activity, we learn from nature how to use molecules or biological nanostructures to build materials with specific features. The focus is on understanding the properties of colloids of biological origin, the dynamics at the bio-interfaces, the strength and stability of natural structures. The final goal is to transfer the acquired knowledge on innovation by developing sustainable and smart materials and processes.

Experimental facilities

The NL facilities allow for detailed experimental studies in nanoscience, photonics and biotechnologies. Since the effective collaboration with FBK most material processing and device productions are performed within their premises. For photonics, we have facilities to cover the light spectrum from the THz to UV ranges with whatever time resolution is needed. Laser sources comprehends: Ti-sapphire fs-ps laser (1 W average over 1000-700 nm, 2 ps or 70 fs pulses, 82 MHz repetition rate); four tunable fiber pigtailed CW lasers (850-870 nm, 1200 - 1700 nm and 1500 - 1600nm); high power fiber-laser at 1550 nm (1-100 MHz, 50 ps); 4W EDFA and 2W semiconductors amplifiers; a supercontinuum light source (410-2400 nm, 1W); several pigtailed diode lasers; ASE source at 1550 nm and a broad band SLD at 800 nm; MIR laser; frequency stabilized 7550 nm laser; high-power true-CW DPSS single-line laser operating at 532, 473 and 355 nm. Detectors comprehend: visible and infrared photomultipliers and CCDs, avalanche photodiodes for vis and IR ranges plus many single photon detectors in the visible and IR. Two homemade MIR single photon-counters. To perform spectral analysis several setups are available: FTIR and dispersive spectrophotometers, a micro-Raman setup, a micro-FTIR and a UV-vis-IR spectrophotometer (shared with other laboratories), UV-Vis and fluorescence spectrophotometer dedicated to biochemical experiments. Nine set-ups are dedicated to the characterization of photonic integrated circuits, equipped with nanopositioning systems and polarization controllers, each specified on a given function: visible, visible broad range, quantum, passive infrared, high speed infrared, non-linear infrared, non-linear MIR and on wafer. A set-up is dedicated to high speed telecom measurements, with 80 Gbps capability where a 60 GHz arbitrary waveform generator, electro-optical modulators, coherent detectors and a four channels, 20 GHz oscilloscope. A 125 km single mode fiber link with optical switches, preamplifiers and dispersion compensation unit is also available. Other devices are: - a solar simulator for cells up to 5 inches in size; - two nanoprobe stations (AFM and SNOM) - two semiconductor probe stations (4 and 8 inches) and different electrical characterization systems (I-V, Z-Ω, EL-I, etc.). Four VIS to NIR optical spectrum analyzers are available. A probe station is interfaced by a fibres bundle with a spectrometer equipped with nitrogen cooled visible and IR CCDs. An electrochemical laboratory with various chemical hoods, galvanostats and volt-ameters is available for sample processing. For optical, electrical and molecular dynamics simulations, the laboratory uses free and commercial software and has work-stations with 4 GPU. Two laboratories are also available, one dedicated to chemical synthesis and the other to the preparation of biological samples. Two other laboratories with biological hoods, incubators and confocal microscopes are dedicated to biological experiments. In one, a confocal microscope with an insert for electrophysiology (MEA) and optogenetics measurement equipped with a "spinning disk" system for fast acquisitions and a super-resolution system.

2023 Publications

• Emiliano Staffoli, M Mancinelli, Paolo Bettotti, and Lorenzo Pavesi “Equalization of a 10 Gbps IMDD signal by a small silicon photonics time delayed neural network”, Photonics Research 11, 878-886 (2023).

• Riccardo Franchi, Stefano Biasi, Diego Piciocchi, and Lorenzo Pavesi “The Infinity-loop microresonator: a new integrated photonic structure working at an exceptional point”, APL Photonics 8, 056111 (2023).

• Nicolò Leone, Stefano Azzini, Sonia Mazzucchi, Valter Moretti, Matteo Sanna, Massimo Borghi, Gioele Piccoli, Martino Bernard, Mher Ghulinyan, and Lorenzo Pavesi, "Generation of quantum-certified random numbers using on-chip path-entangled single photons from an LED," Photon. Res. 11, 1484-1499 (2023).

• Jong-Moo Lee, Alessio Baldazzi, Matteo Sanna, Stefano Azzini, Joon Tae Ahn, Myung-Lae Lee, Youngik Sohn, and Lorenzo Pavesi, "Do different kinds of photon-pair sources have the same indistinguishability in quantum silicon photonics?" Photonics Research 11, 1820-1837 (2023).

• Stefano Biasi, Riccardo Franchi, Lorenzo Cerini, and Lorenzo Pavesi “An array of microresonators as a Photonic Extreme Learning Machine”, APL Photonics 8, 096105 (2023).

• Matteo Sanna, Davide Rizzotti, Stefano Signorini, and Lorenzo Pavesi “2 µm Ghost Spectroscopy with an Integrated Silicon Quantum Photonics Source” Advanced Quantum Technologies 2300159 (2023).

• Ilya Auslender, Yasaman Heydari, Clara Zaccaria, Asiye Malkoç, Beatrice Vignoli, and Lorenzo Pavesi "An integrated setup for in-vitro optogenetic experiments using AI to localize stimulation", Proc. SPIE 12366, Optogenetics and Optical Manipulation 2023, 1236609 (14 March 2023).

• M. Sgritta, B. Vignoli, D. Pimpinella, M. Griguoli, S. Santi, A. Bialowas, G. Wiera, P. Zacchi, F. Malerba, C. Marchetti, M. Canossa, E. Cherubini “Impaired synaptic plasticity in an animal model of Autism exhibiting early hippocampal GABAergic-BDNF/TrkB signaling alterations” iScience, 26(1), 105728 (2023).

• Chiara Michelini, Stefano Signorini, Valerio Pruneri, and Lorenzo Pavesi “Undetected photon interference measurements on a silicon chip” Proc. SPIE 12692, Quantum Communications and Quantum Imaging XXI; 126920F (2023).

• I. Auslender and L. Pavesi, "Reservoir Computing Model For Multi-Electrode Electrophysiological Data Analysis," 2023 IEEE Conference on Computational Intelligence in Bioinformatics and Computational Biology (CIBCB), Eindhoven, Netherlands, 2023, pp. 1-6.

• Emiliano Staffoli, Davide Bazzanella, Stefano Biasi, Giovanni Donati, Mattia Mancinelli, Paolo Bettotti, and Lorenzo Pavesi “Nonlinear response of Si Photonics resonators for reservoir computing neural network” in Advances in optical communications: from integrated photonics to optical systems and networks, CNIT Technical Report 12 edited by Marco Romagnoli, Marco Secondini and Massimo Tornatore, (Texmat 2023) pag 3-34 ISBN:

9788894982794 DOI: 10.57620/CNIT-Report_12.

• Giuseppe Cantarella, Mallikarjun Madagalam, Ignacio Merino, Christian Ebner, Manuela Ciocca, Andrea Polo, Pietro Ibba, Paolo Bettotti, Ahmad Mukhtar, Bajramshahe Shkodra, AKM Sarwar Inam, Alexander J. Johnson, Arash Pouryazdan, Matteo Paganini, Raphael Tiziani, Tanja Mimmo, Stefano Cesco, Niko Münzenrieder, Luisa Petti, Nitzan Cohen, Paolo Lugli "Laser-Induced, Green and Bio-compatible Paper-Based Devices for Circular Electronics." Advanced Functional Materials 33, 2210422 (2023).

• Nardi, M.V., Froner, E., D'Amato, E., Timpel, M., Scarpa, M., Verucchi, R., "Quantification of carboxylic binding sites on functionalized silicon nitride surface through X-ray photoelectron signal and fluorescence labelling" Current Applied Physics, 56, pp. 111-118 (2023).

• Nardi, M.V., Timpel, M., Pasquardini, L., Toccoli, T., Scarpa, M., Verucchi, R., "Controlled Carboxylic Acid-Functionalized Silicon Nitride Surfaces through Su-personic Molecular Beam Deposition" Materials, 16 (15), art. no. 5390 (2023).

2023 Patents

Sistema per la generazione e lo scambio di chiavi sicure quantistiche basate sull'entanglement a singolo fotone (inventori Pavesi Lorenzo, Mazzucchi Sonia, Azzini Stefano, Leone Nicolò) domanda IT 102023000024174 del 15/11/2023

2023 PhD Thesis

"A time-delay reservoir computing neural network based on a single microring resonator with external optical feedback", Giovanni Donati (defense 28 July 2023)

"The taiji and infinity-loop microresonators: examples of non-hermitian photonic systems", Riccardo Franchi (defense 1 june 2023)

Project web sites

http://nanolab.physics.unitn.it/

https://r1.unitn.it/back-up/

https://epiqus.fbk.eu/

https://r1.unitn.it/pelm/

https://sites.google.com/unitn.it/panacea/home

https://www.quantumtrento.eu/

1. Using Hermitian and non-Hermitian microresonators for local perturbation sensing (Stefano Biasi, Riccardo Franchi)

To detect small local perturbations, such as the presence of a molecule/particle, several techniques have been developed in integrated photonics. The most traditional ones involve the use of unbalanced Mach–Zehnder interferometers or microresonators, where one observes the shift in resonant frequency caused by the small perturbation due to the local variation of the waveguide refractive index. More recent techniques aim to observe how the local perturbation changes the coupling between the two internal counterpropagating modes in a microresonator. In fact, the coupling between these modes causes a splitting of the spectral response, transforming the typical Lorentzian dip in a doublet, whose splitting reflects the strength of the perturbation.
To further improve this technique, not only Hermitian but also non-Hermitian microresonators have been studied. A fundamental difference between these two systems concerns the degeneracies of the modes. In the Hermitian case, the degeneracies are called Diabolic Points (DPs), and the splitting of the eigenvalues, which is closely related to the splitting of the spectral response, exhibits a linear trend as a function of the perturbation strength. In contrast, in the non-Hermitian case, the degeneracies are called Exceptional Points (EPs), and the splitting follows a square root dependence as a function of the perturbation. This difference leads to a larger sensitivity of EP than of DP for small perturbations.
We have studied silicon-integrated microresonators (MRs) at either a DP or an EP to compare their sensistivity. One way to make a MR at an EP is to insert an S-shaped waveguide inside it to create an asymmetric coupling between the counterpropagating modes. This microresonator is called a taiji microresonator (TJMR) and its design is shown in Fig. 1(c). If we remove this asymmetric coupling between the two modes of the system, it becomes a Hermitian system at a DP. Both a MR, see Fig. 1(a), and a TJMR with an S-shaped waveguide cut (TJMR-cut), see Fig. 1(b), can be realized. In particular, the realization of TJMR-cut and TJMR is very relevant for their comparison, since they operate at different points but have the same losses.
In order to compare the sensitivity of these MRs, for each type of MR we fabricated six different configuration of an integrated scatterers capable of simulating the presence of a local perturbation inside the MR. To create these integrated scatterers while respecting the fabrication constraints, we designed by COMSOL Multiphysics® a circular hole of various diameters *d={0, 0.14, 0.16, 0.18, 0.20, 0.22}* µm inside the waveguide of the microresonator, see Fig. 1(d). Figure 1(d) shows how the field coming from the left is retroreflected by the hole, creating interference patterns.

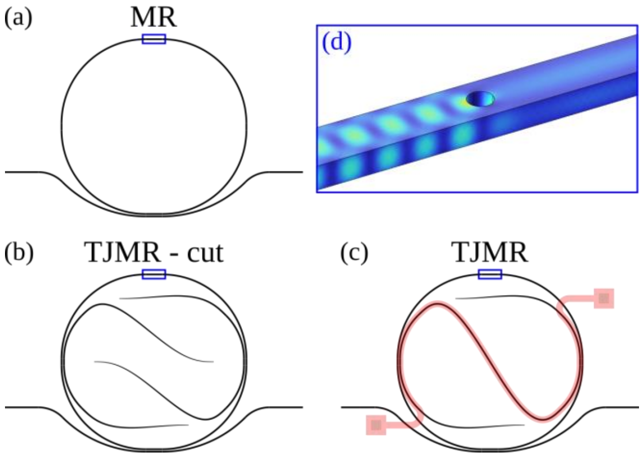

Figure 1: *Sketch of a microring resonator (a), a taiji microresonator with the S-shaped waveguide cut (b), and a taiji microresonator (c). (a) and (b) represent microresonators at a DP, instead (c) one at an EP. (d) Simulation of a waveguide with a hole in the center. The simulation is performed with the excitation coming from the left. The blue rectangles in (a)-(c) indicate the regions where the scatterer/hole is inserted. The red line in (c) represents a microheater.*

We are currently measuring these different devices on different optical chips to gather sufficient statistics. The latter is also necessary because we have observed experimentally that the fabrication of holes inside the waveguides has reproducibility problems. Moreover, for the first time, thanks to the presence of a microheater realized above the S-shaped waveguide, the red line in Fig. 1(c), it will be possible to tune the sensitivity of the TJMR in such a way as to obtain its maximum performance.

2. An integrated device for controlling energy exchange between counterpropagating modes (Stefano Biasi, Riccardo Franchi, Bülent Aslan, Salamat Ali)

In quantum physics, conservation of energy requires a closed system to have real eigenvalues. Therefore, physical models are based on mathematical hermiticity, meaning that the system is isolated from its environment. However, a more realistic model often requires the description of part of the system. In these cases, energy may be exchanged between the specific subsystem and the environment. Thus, non-conservative elements and consequently a non-Hermitian Hamiltonian must be considered. Non-Hermitian Hamiltonians govern optics by nature. The radical difference between non-Hermitian and Hermitian occurs in the presence of degeneracies. In the case of Hermitian Hamiltonians, the three-dimensional space of eigenvalues is a function of two dependent parameters forming a double-cone topology (a diablo) where the cones touch at their apex and form a diabolic point. Here, the eigenvectors remain orthogonal as the degeneracy approaches. In contrast, non-Hermitian matrices have a complex topology of two intersecting Riemann sheets centered on degeneracies, so called exceptional points, in the three-dimensional space of eigenvalues. Here, unlike in the diabolic point, not only the eigenvalues but also the eigenvectors coalesce as the degeneracy approaches. Optical structures operating near these points have led to the demonstration of non-trivial effects such as unidirectional invisibility and non-reciprocal propagation of light. Consequently, the study of the behavior of systems operating near degeneracies has become fundamental.

In this work, we study the response of a reconfigurable integrated optical system that allows the reproduction of different topologies of double-cone or Riemann surfaces, allowing the study of both diabolic and exceptional points. It consists of a typical microresonator coupled to a bus waveguide that also has a two-lobe coupling, see Fig. 2.

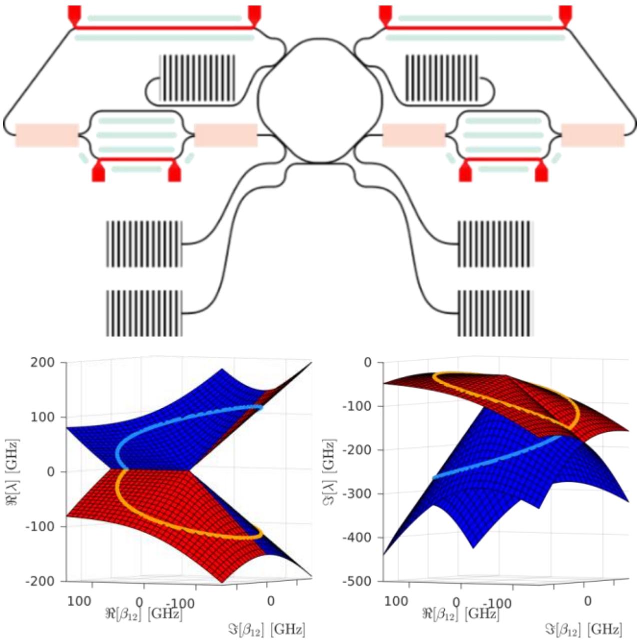

Figure 2: *Top, design of the optical device that allows the control of the energy exchange between the counterpropagating modes. Bottom, real and imaginary parts of the eigenvalues as a function of the real and imaginary parts of the coupling coefficients between the counterpropagating modes. The red and blue colors highlight the two different eigenvalues. The two circular orange and cyan lines on the eigenvalue plots show the path followed on the sheets when the current is applied only on the phase shifter of the left lobe.*

The diametrically opposed lobes allow part of the energy of a mode circulating in the microresonator to be extracted and re-injected by reversing the direction of propagation. This creates a coupling between counterpropagating modes that can be controlled by a Mach-Zehnder interferometer and a phase shifter located on both lobes. Both the interferometer and the phase shifter are actuated by applying current to metal microheaters. For example, by simply setting the destructive interference on one of the Mach-Zehnders of the two lobes, it is possible to mimic the unidirectional reflector behavior of a Taiji microresonator. By measuring the spectral response as the configurations of the phase shifters and/or Mach-Zehnder change, it is possible to reconstruct the trend of the eigenvalues as a function of the real and imaginary parts of the counterpropagating mode coupling coefficients. The bottom panel of Fig. 2 shows an example of surfaces in the complex plane obtained in the Hermitian configuration. The paths shown are the operating points that can be obtained simply by varying the current applied only to the left-lobe phase shifter. The blue and red colors highlight the two eigenvalues of the system.

3. Coupled Resonators Optical Waveguide based on taiji microresonators (Bülent Aslan, Riccardo Franchi, Stefano Biasi, Salamat Ali)

Physical systems with topological properties are robust against disorder. However, their implementation in integrated photonic devices is challenging because of the various fabrication imperfections and/or limitations that affect the spectral response of their building blocks. One such feature is strong backscattering (BS) due to the surface wall roughness of the waveguides, which can flip the propagating modes to counterpropagating modes and destroy the desired topological behavior. We have studied an integrated photonic structure based on a sequence of two taiji microresonators (MRs) coupled with a middle link MR (a taiji-CROW device, where CROW stands for coupled resonator optical waveguides), Fig. 3. The study provides design constraints to preserve the ideal operation of the structure by quantifying a minimum ratio between the BS and coupling coefficients. This ratio is valuable to avoid surface roughness problems in designing topological integrated photonic devices based on arrays of MRs.

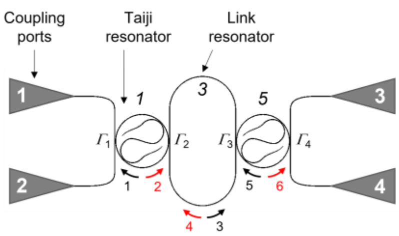

Figure 3: *The taiji-CROW device. Arrows with numbers indicate the propagating fields and the continuing modes in the sequential resonators follow the same color coding: 1 → 3 → 5 are black, and 2 → 4 → 6 are red. Enumerated triangles on both sides represent grating couplers acting as the device's input/output ports. Γs refer to the coupling coefficients.*

This taiji-CROW device also serves as a building block of more complex topological photonic systems and exhibits strong unidirectional reflection by design and a non-reciprocal intermodal coupling due to its non-Hermitian nature. When the input signal is coupled to port-1, only counterclockwise (CCW) modes are excited and the output signal is only detected in port-2 and port-3. On the other hand, when the input signal is coupled to port-2, the S-shaped waveguide allows coupling between the clockwise (CW) and CCW modes and therefore an output signal is observed from all the four device ports. Indeed, the taiji-CROW device can generate different transmission spectra without violating the Lorentz reciprocity theorem at each output port when it is excited from any of the four input ports. For reflection (i.e., the output signal from the same port where the input signal is coupled to), while ports 1&4 exhibit no signal, ports 2&3 produce a strong signal. However, in experiments these properties appeared to be weakened (if not totally diminished) due to the existence of the strong BS in the structure.

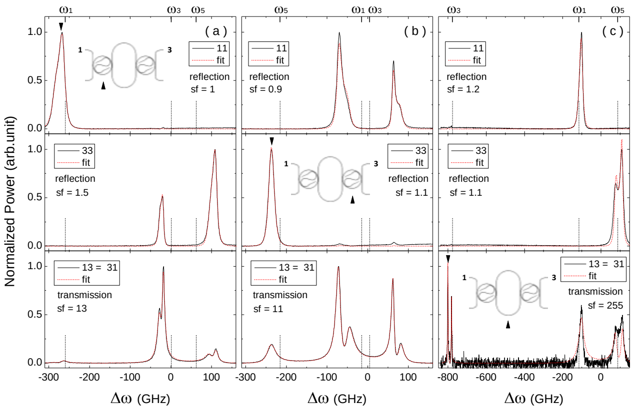

Figure 4: *Measured spectra (black line) and fit (dashed red line) for three different devices, which have one resonant frequency very different from the others. The top (middle) panels refer to the 11 (33) reflection. The bottom panels refer to the 13 or 31 transmission. The insets show the taiji-CROW device with an arrow pointing to the MR which is responsible for the marked low frequency peak. The vertical dashed lines indicate the resonant frequencies of each MR. "sf" stands for the scale factor.*

The spectral properties of the fabricated structures were investigated in the linear optical regime. Figure 4 shows the transmission and reflection spectra for three different devices with different resonance conditions. The optical signal was input from port-1 or port-3. For each device, the transmission spectra (13 or 31, where the first number refers to the input port and the second to the output port) are identical while the reflection spectra (11 or 33) are different. Three main peaks are observed, each split or broadened by a significant BS from the waveguide surface-wall roughness. BS is also the cause of the strong reflection observed from port-1. The observed characteristics were then modeled and analyzed in terms of the physical properties using the Temporal Coupled Mode Theory to describe the light propagation behavior in the taiji-CROW: the dashed red lines in Fig. 4 show the fitting results. To mitigate the effect of BS, one can either reduce it (e.g., by modifying the waveguide geometry, material, and the fabrication method) or increase the coupling between the different MRs but this means compromising on the quality factor. Specifically, we found that $|\beta_{BS}|/\Gamma \lesssim 0.17$ is the onset value for mode splitting which indicates strong BS. Here, β_{BS} and Γ are the BS and coupling coefficients, respectively. From the experimental results, we find this ratio to be ~1.5±1.1 indicating that our devices under test operate in the large backscattering regime.

4. Three coupled waveguides for photon routing in integrated optical circuits (Salamat Ali, Stefano Biasi, Riccardo Franchi, Bülent Aslan)

In integrated photonics, precise control of light signals plays a pivotal role. Light routing within photonic devices typically relies on multi-mode interferometers and microresonators. However, n × n waveguide couplers present a viable alternative. Here, we investigate both theoretically and experimentally the use of 3 × 3 devices in achieving a versatile tunable switch, where light can be routed from each input port to any output port.

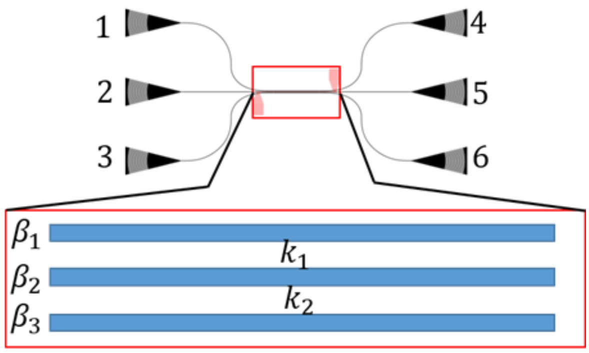

Figure 5: *Three coupled waveguides.*

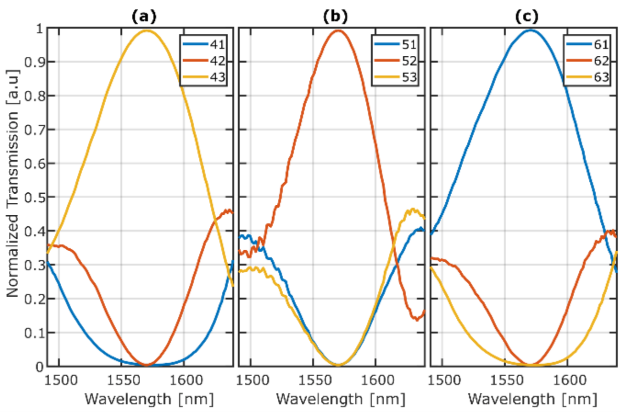

Figure 6: *Experimental results for power switching for different wavelengths in a 3X3 structure.*

We experimentally measured 3x3 couplers with various waveguide lengths and different inter-waveguide distances (Fig. 5). The experiments also include measurements on a 3x3 coupler with a heater mounted on the middle waveguide to tune the propagation constant and the effective coupling coefficients. We demonstrated that the device, when no current is applied on the heater, can transfer the signal from the external waveguide while keeping the central waveguide unchanged, or even achieve a balanced output across all three output ports. This includes direct routing (from port 4 to 2), signal splitting (from port 4 to ports 1, 2, and 3), and cross-routing (from port 4 to 3 and port 6 to 1), along with any arbitrary combination of these paths as shown in Fig. 6.

In quantum mechanics, the Bloch sphere provides a geometrical representation of a two-level system. It is represented as a unit sphere where each point on the surface corresponds to a potential state of the qubit. In contrast, a qutrit extends the concept of a qubit to a three-level system. A qutrit can exist in a superposition of three states, denoted as $|1\rangle$, $|2\rangle$, and $|3\rangle$. Within three coupled waveguides, a qutrit's state can be represented by the distribution of light's amplitude or power across the three waveguides. Each waveguide is associated with one of the qutrit's basis states. The state of the photon in this view is a linear combination of these basis states: $|\psi\rangle = a_1|1\rangle + a_2|2\rangle + a_3|3\rangle$, where $|\psi\rangle$ is the qutrit's state vector, a_1, a_2 and a_3 are complex coefficients ($|a_1|^2+|a_2|^2+|a_3|^2 = 1$). Using the 3x3 coupler it is possible to represent the qutrit in a Bloch sphere where each waveguide serves as a potential path for the photon, allowing it to exist in one waveguide, in a superposition of two, or in a superposition across all three waveguides.

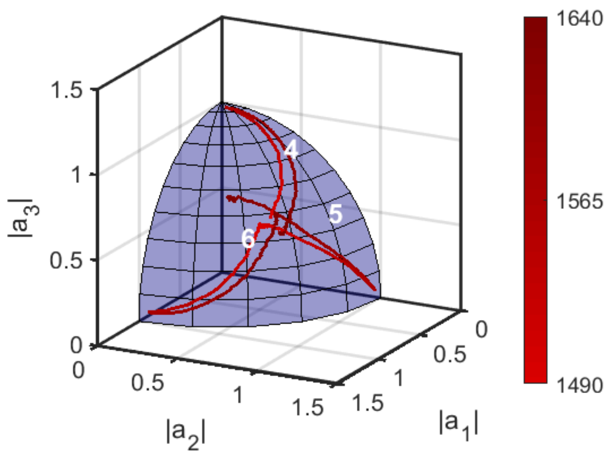

Figure 7: *One-to-one correspondence with a 3D Bloch Sphere based on the power in each waveguide. Here, a_i is the square root of the power measured at port i.*

Figure 7 shows the excitation of ports 4, 5, and 6 at zero voltage covering a wavelength range from 1490 nm to 1640 nm. This corresponds to a range of coupling values. Note that the sum of the powers invariably equals unity. As a result, for any given coupling value, the points representing different combinations are positioned on the surface of a unit sphere. These combinations originate from nearly the same distance but diverge in various directions, each path being distinctively influenced by the respective coupling values. This divergence results in traversing different areas on the sphere's surface, effectively covering various parts of the sphere for the different coupling values. Subsequently, the points re-converge, almost returning to their initial positions.

5. Toward microresonator-based spiking neural networks (Stefano Biasi, Alessio Lugnan, Davide Micheli)

Microresonators are one of the fundamental building blocks of integrated photonics. One of their strengths lies in their ability to store a high field intensity, which enhances nonlinear effects. This makes the nonlinear response available at relatively low input powers. Thus, in the case of silicon microresonators, one can demonstrate bistable behavior based on either the thermal-optical nonlinear effect or the free-carrier dispersion effect, where free carriers are generated by two-photon absorption. These two nonlinearities differ for the timescale and influence on the resonance wavelength. The combination of thermo-optic and free-carrier effect generates self-pulsing behavior. In this case, a constant input is converted into an oscillating periodic signal. It has been shown that the nonlinear dynamics of a single microresonator can emulate major neurocomputational properties, paving the way for the creation of complex topological architectures for artificial spiking networks based on microresonators.

Here, we study the experimental response in the self-pulsing regime of Side-Coupled Integrated Spaced Sequence of Resonators (SCISSOR) composed of one, two and three rings, respectively. In particular, we show that it is possible to obtain self-pulsing responses with different oscillation periods and/or patterns by varying the power and frequency of the input laser. Figure 8 shows an example for the drop port response of the single microresonator. At the top, the blue line shows the spectral response in the linear regime (low power), while the color map shows the lowest frequency of self-pulsing oscillations as a function of the power and frequency of the input laser. The four graphs labeled spiral, star, square, and dot show, with the red line, the time response associated with a particular point on the map. The black dashed line represents a sinusoidal function, which oscillates with the self-pulsing frequency of the color map. The spiral, a point in the color map at low input power, represents the low power transmission, which reflects the lineshape of the input signal. It represents a deformed square wave due to the optical modulator. However, the exponential decay at the transition times enriches the microresonator dynamics by highlighting its sensitivity to variations. When in the self-pulsing regime, a simple microresonator exhibits a complex behavior, ranging from a typical self-pulsing pattern (graph labeled with star) to an irregular pattern with varying distances between peaks (graph labeled with square), to a fast sinusoidal-type oscillation (graph labeled with dot). The dynamics are greatly enriched by increasing the microresonator number in the SCISSORS, showing complex patterns and oscillations with frequencies almost three times larger than those obtained by a single microresonator. We explored the possibility of using these self-pulsing states to create long-term memories, i.e., far greater than the typical fading memory result due to the thermo-optic effect. Finally, we tested the ability of a SCISSOR to detect spike sequences at different frequencies using self-pulsing states to verify its use as a building block for implementing a spiking neural network.

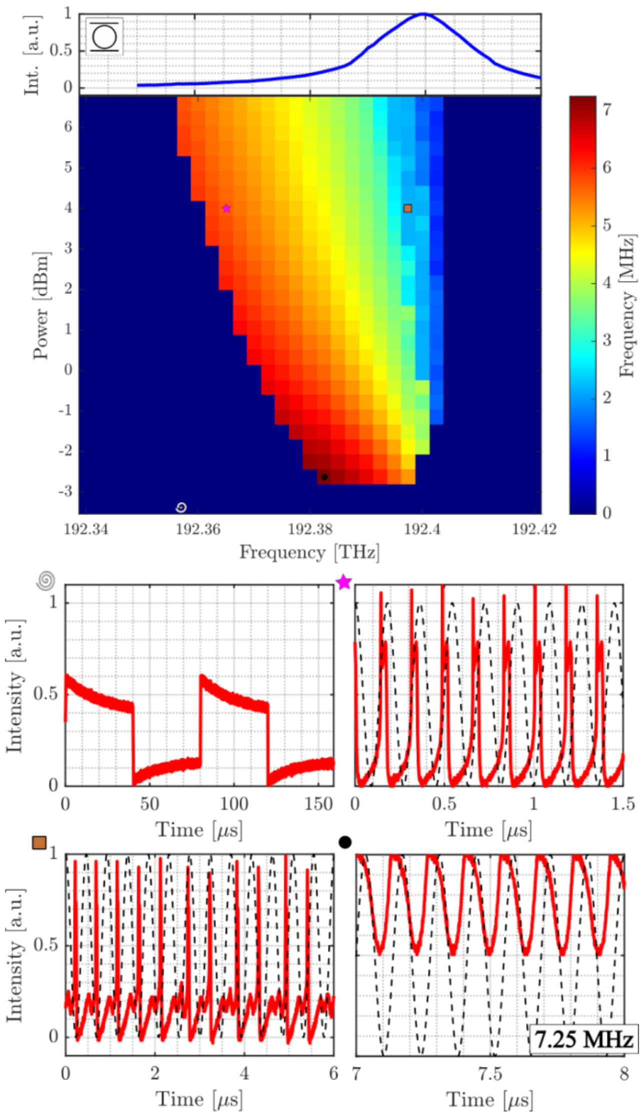

Figure 8: *Spectral and temporal response of the drop port of a microresonator. The spectral response at low power is shown at the top. The color map in the middle shows the oscillation frequency of the self-pulsing states as a function of frequency and power of the input laser. At the bottom, four graphs show the time response at a given point on the color map, labeled spiral, star, square, and dot.*

6. Time-delay reservoir computing with a single microring resonator: experiment (Giovanni Donati)

A single microring resonator is coupled to an optical fiber feedback loop to investigate information processing based on time-delay reservoir computing (RC). According to this processing scheme, each information to be processed is nonlinearly transformed by the system's nonlinear response, which is then used to sample a set of virtual nodes. A final readout layer receives as input the virtual nodes' state and performs a (trained) weighted sum to achieve the target of interest. Here, the input optical bit is pre-processed using a mask (M), and the nonlinear output response is encoded at the drop port (highlighted in green in Fig. 9), therefore subject to the microring and detection nonlinearities. Thanks to the external feedback, the response at the drop port accounts for past information, thus promoting the study of the system on memory-demanding tasks.

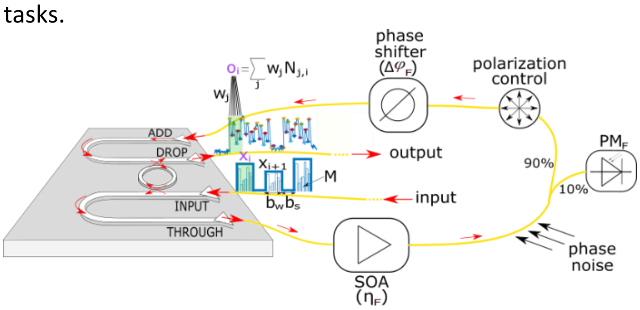

Figure 9: *Microring resonator coupled to an external fiber-based optical feedback, along with instruments that are used to tune the strength (η_F) and phase ($\Delta\phi_F$) of the delayed information. b_w:bit duration; b_s: bit separation time; M:mask; x_i: input information to be processed; w_j: trained output weights; o_i: computed output, $N_{j,i}$: virtual node states; PM_F: monitor detector.*

Delayed boolean benchmark tasks confirmed the fiber-based feedback as a consistent source of optical memory for the system. The investigation is now extended to the Santa Fe and Mackey Glass benchmark prediction tasks, still exploring different critical system parameters such as the input optical power (P_{in}), the detuning between the pump and the cold microring resonance wavelengths ($\Delta\nu_s$), the feedback strength (η_F-Soa current) and phase ($\Delta\phi_F$). The task performances on the Santa Fe task are expressed in Fig. 10 (a) via the normalized mean square error (NMSE), and as a function of the input optical power, when using only 7 virtual nodes, bit duration b_w=77 ns, and feedback delay τ_F=88 ns. In this case, the best score requires a precise amplification of the feedback signal, as shown in Fig. 10 (b). The task is then repeated for a larger number of virtual nodes (38) by extending the feedback delay, and therefore the fiber length, with the results reported in Fig. 10(c). In this scenario, the feedback signal becomes unreliable due to a stronger environmental noise, which is no longer compensated by the phase controller designed for this experiment. All results in Fig. 10(c) are indeed found for zero

SOA current, where the feedback signal is mostly attenuated. According to Fig. 10(c), the single microring allows as well to solve the task, thus meeting its memory requirements, without the feedback support. To test experimentally whether the microring nonlinearities were acting as a source of memory during the task, the system is set in the best configuration in Fig 10(c) (P_{in}=0.85 mW, $\Delta\nu_s$=0) and the task is repeated for different input bit separation times (b_s in Fig 9): if the bit separation is large enough, the free carrier and temperature variations induced in the microring waveguide, when encoding the optical input bit x_i, will relax completely before the next optical pulse x_{i+1} is injected. Thus, no trace of the previous information is stored in the microring when the next optical pulse propagates through it, with consequent loss of the microring nonlinear memory.

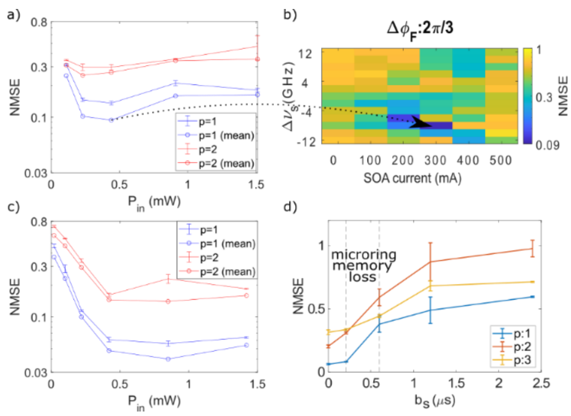

Figure 10: *Performance obtained in the Santa Fe task in terms of NMSE. a) NMSE dependence on the input optical power, when using 7 virtual nodes and the feedback. b) The parameter space, defined by the detuning and feedback strength (SOA current) where the best performance in a) is found. c) NMSE performances of the single microring in the absence of optical feedback, with 38 virtual nodes. d) NMSE results obtained when setting the system in the best configuration in c), and repeating the task for different input bit separations. The task is repeated for different prediction steps ahead (p). The term mean in the legend refers to a unique NMSE estimated from the average of the optical traces acquired per measure.*

Fig. 10(d) confirms that the task performances (NMSE) are preserved when b_s<0.21 μs, and then degraded for longer b_s values, where the memory is lost. This time may be indeed linked to both the slow decay rate of the free carrier population and the longer thermal lifetime. These results are indeed achieved under a self-pulsing dynamics. Similarly, the Mackey Glass task is solved when using 7 virtual nodes when relying also on the feedback information, but it is not improved when using the single microring alone, even when the number of virtual nodes is increased to 38.

7. High-speed image processing with microresonators on a photonic chip (Alessio Lugnan, Stefano Biasi)

Optical fibers are employed all around the world as telecom links and in data centers to transmit data at high throughput. However, nowadays most of the data processing is performed by electronics, requiring costly and power-hungry conversions between the optical and the electrical domains. Photonic neuromorphic computing systems (e.g. optical artificial neural networks on a photonic chip) allow keeping all or part of the required data processing for machine learning applications in the optical domain. Furthermore, they present advantages in terms of latency, energy consumption and throughput with respect to their electronic counterparts.
Here, we employ silicon microring resonators (MRRs), as artificial neurons to build energy efficient and high-throughput physical neural networks. MRRs enable multi-wavelength operations, allowing us to deploy a large network within a much smaller physical topology. Moreover, we exploit silicon nonlinear effects, based on temperature and free carriers of the MRRs, so as to generate extremely complex network dynamics that can be used to increase the computational power of computationally cheap machine learning models (according to the *reservoir computing* paradigm).

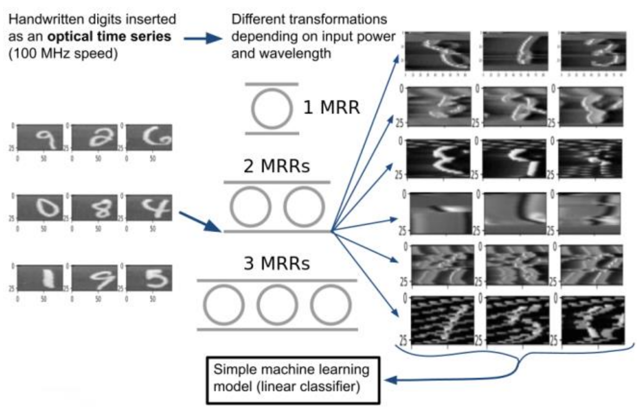

Figure 11: *Diagram of the measurements. Handwritten digits from the MNIST dataset (left) are inserted as an optical time series (wavelength around 1550 nm) into networks of 1, 2 and 3 MRRs (center). Several different nonlinear image representations (right) are obtained from each structure. These representations can be used to boost the computational power of an efficient machine learning classifier.*

We considered the machine learning classification of tens of thousands of handwritten digits (MNIST dataset) as a benchmark task. We inserted these images into small networks of 1, 2 and 3 coupled MRRs (Figure 11) and collected the corresponding output nonlinear image representations, for different input wavelengths and optical powers. Then, we tested how useful these representations can be for the considered classification task, when they are fed into a simple and efficient machine-learning model (logistic regression). We obtained accuracies of about 92.5 % for both networks with 1 and 2 MRRs, and of over 93% for the network with 3 MRRs. This shows that the computational power can be enhanced by increasing the number of artificial neurons. As a next step, we are performing similar measurements on networks comprising several tens of MRRs, expecting a significant increase in machine learning performance. In addition, we plan to employ these photonic neural networks for a more practical application, namely as an all-optical efficient processor for fiber sensors (i.e., optical fiber used as sensors, e.g., for vibrations or temperature over long distances).

8. A photonic neural network for impairment compensation in optical telecom links (Emiliano Staffoli, Maddinelli)

Modulated optical signals propagating in fiber are affected by distortions induced by linear effects, among which one of the most severe is represented by chromatic dispersion (CD). This alters the shape of the optical pulses traveling in fiber, generating an intersymbol interference between adjacent pulses and causing a loss of information between the transmitter and the receiver. This in turn implies the necessity of distortion compensation along the propagation path. To compensate or correct for CD, several types of equalization techniques have been introduced, with dispersion compensating optical fibers and Bragg gratings being the most diffused ones. An alternative solution is proposed by the University of Trento with the ALPI project, which intends to use integrated Photonic Neural Networks (PNNs) to recognize and compensate distortions in optical signals. The advantages in the adoption of this technology derive from operating the corrections directly on the optical sequence, drastically reducing the latency as well as increasing the flexibility of the equalization, which can be learned directly on the deployed link and, therefore, can be easily adapted to optical link variations.

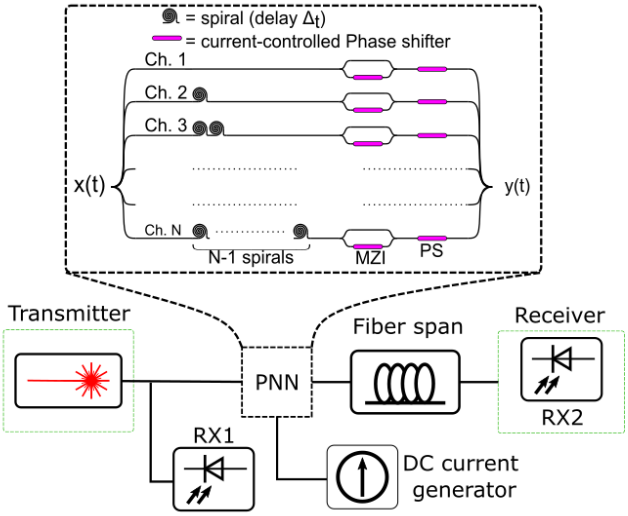

Figure 12: *Experimental setup. Light is generated and modulated in the transmission stage and then sent to the PNN for optical processing. The amplitude and phase weights are controlled by metallic heaters (purple lines) placed on top of the Si waveguides. The signal proceeds then into an optical fiber span. Two fast photodiodes monitor the input (RX1) and the output (RX2) signals.*

The PNN device is based on a *N*-channel Delayed Complex Perceptron, whose schematic is shown in Figure 12. It is fabricated on a Silicon-on-Insulator platform, with Si waveguides surrounded by Silica claddings. The PNN device transforms an input sequence *x(t)* (propagating field) in an output sequence *y(t)* according to

$$y(t) = \sum_{i=1}^{N} x[t - \Delta t(i-1)] a_i e^{i\phi_i}$$

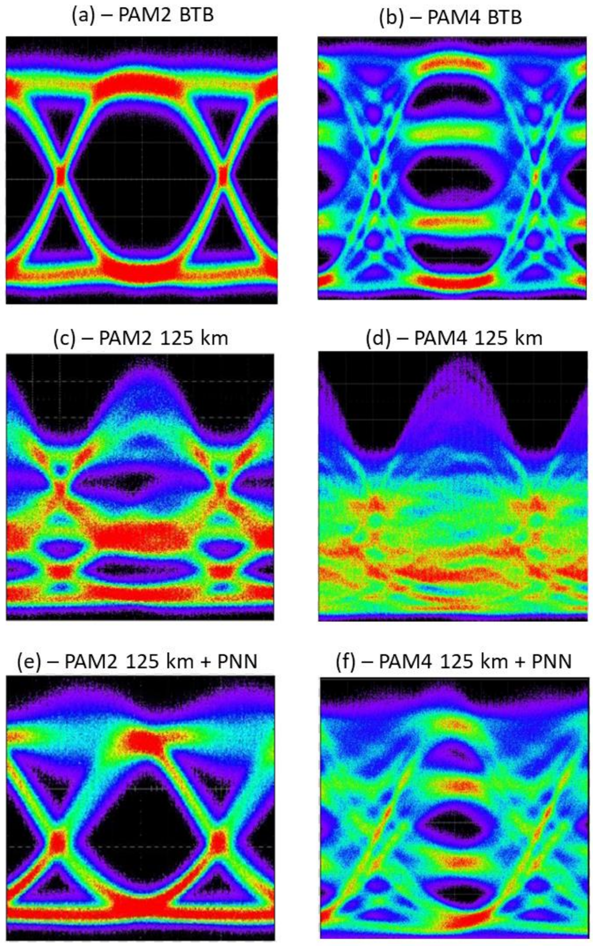

Figure 13: *Eye diagrams at the receiver for 10 GBaud/s PAM2 (a,c,e) and PAM4 (b,d,f) respectively in Back-To-Back(BTB) (a,b), 125 km unequalized (c,d) and equalized (e,f) transmission.*

The signal *x(t)* is split into *N* parallel waveguides and the copies then accumulate a relative time delay multiple of Δt by propagating in spiralized optical paths. An amplitude (a_i) and a phase weight (ϕ_i) are then applied independently to each channel by a cascade of a Mach-Zehnder interferometer (MZI) and a phase shifter (PS). These are controlled by electrical currents flowing on metallic heaters placed on top of the waveguides. The *N* weighted copies are then complex-summed to give *y(t)*. The nonlinear stage of the

PNN is represented by the square modulus operation $|\cdot|^2$ performed by the end-of-line photodiode. The PNN device is inserted in the transmission line presented in Fig. 12.
The training is performed offline via the Particle Swarm Optimizer and aims to create the maximum contrast between the distributions of acquired samples associated with each expected optical level. This leads also to a Bit-Error-Rate (BER) reduction. A visualization of the contrast between the optical levels is provided by the eye diagram. Figure 13 (a-b) show the eye diagram acquired for Back-To-Back transmission, namely signal propagation through a 0 km fiber, which result in a null BER and is taken as the reference Transmitter/Receiver performance. The trained PNN provided CD compensation for 10 Gbps PAM2 and 20 Gbps PAM4 signals propagating up to 125 km fibers, with an average excess loss for the device amounts to 15 dB. Figure 13 shows the comparison between unequalized (c,d) and equalized (e,f) transmission for PAM2 and PAM4 signals. The action of the PNN restores the aperture of the eye diagram, allowing for a clearer distinction between the optical levels and the definition of a threshold which provides null BER after the digitization.
In a collaboration with the Telecommunication Laboratory (LabTel) at the Federal University of Espirito Santo in Brazil (UFES), we aimed at demonstrating that the device performs well with another modulation format, Orthogonal Frequency Division Multiplexing (OFDM). As the name suggests, OFDM is a form of frequency division multiplexing, meaning that the information is encoded on carriers at different frequencies. This is achieved via Digital Signal Processing (DSP) by means of the Fast Fourier Transform (FFT) algorithm. The encoding/decoding procedure is illustrated in Fig. 14. The digital sequence is encoded according to an arbitrary scheme, in our case Quadrature Amplitude Modulation with four symbols (4-QAM). Next, the sequence is divided into frames and each one of them is processed by the inverse FFT. The frames are serialized before the transmission through the optical channel. On the receiver side, demodulation takes place by inverting the operations performed during the modulation.

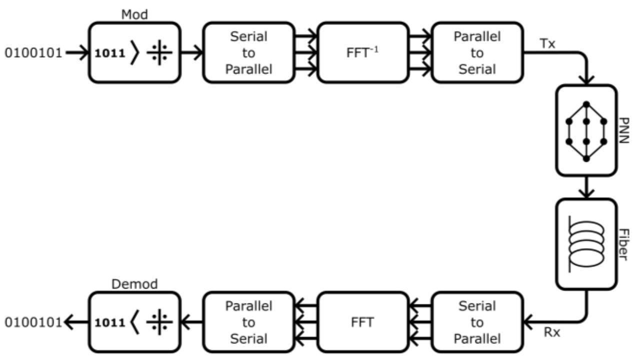

Figure 14: *Block diagram of modulation and demodulation in OFDM.*

The 4-QAM modulation scheme differs from PAM2 or PAM4 in that the information is encoded not only in the amplitude but also in the phase of the signal. The constellation diagram (Fig. 15) shows how pairs of bits are mapped into the amplitudes of the in-phase (I) and quadrature (Q) subcarriers. In a real-world scenario, the mapping into the constellation diagram is subject to noise. The amount of scattering of the actual constellation with respect to the ideal case is quantified by the Error Vector Measure (EVM), which served us as the loss function for the PSO in the training of the PNN. By minimizing the EVM, the BER is minimized as well. The performance of the PNN was tested for different fiber lengths ranging from 25 km to 125 km. As shown in Fig. 15, the constellation diagram after 125 km is heavily degraded by CD, however the trained PNN fully recovers the OFDM signal.

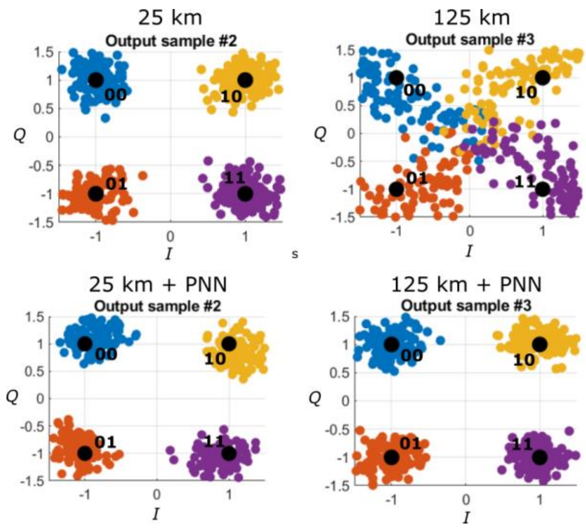

Figure 15: *Constellation diagrams at the receiver at 25 km and 125 km. At 25 km there is no need of compensation because the effect of chromatic dispersion is minimal. At 125 km the PNN successfully recovers the distorted signal.*

9. AI-based model to decode electrophysiological signals of neuronal networks (Ilya Auslender)

The electrophysiological nature of neuronal networks allows revealing various interactions between different cell units at very short time-scales. One of the many challenges in analyzing these signals is to retrieve the morphology and functionality of a given network. In this work, we developed a computational model, based on Reservoir Computing Network (RCN) architecture, which decodes the spatio-temporal data from electro-physiological measurements of neuronal cultures and reconstructs the network structure on a macroscopic domain, representing the connectivity between neuronal units (Fig. 16). The model predicts the connectivity map of the network with higher accuracy than other methods such as the Cross-Correlation and Transfer-Entropy methods (Fig. 17).

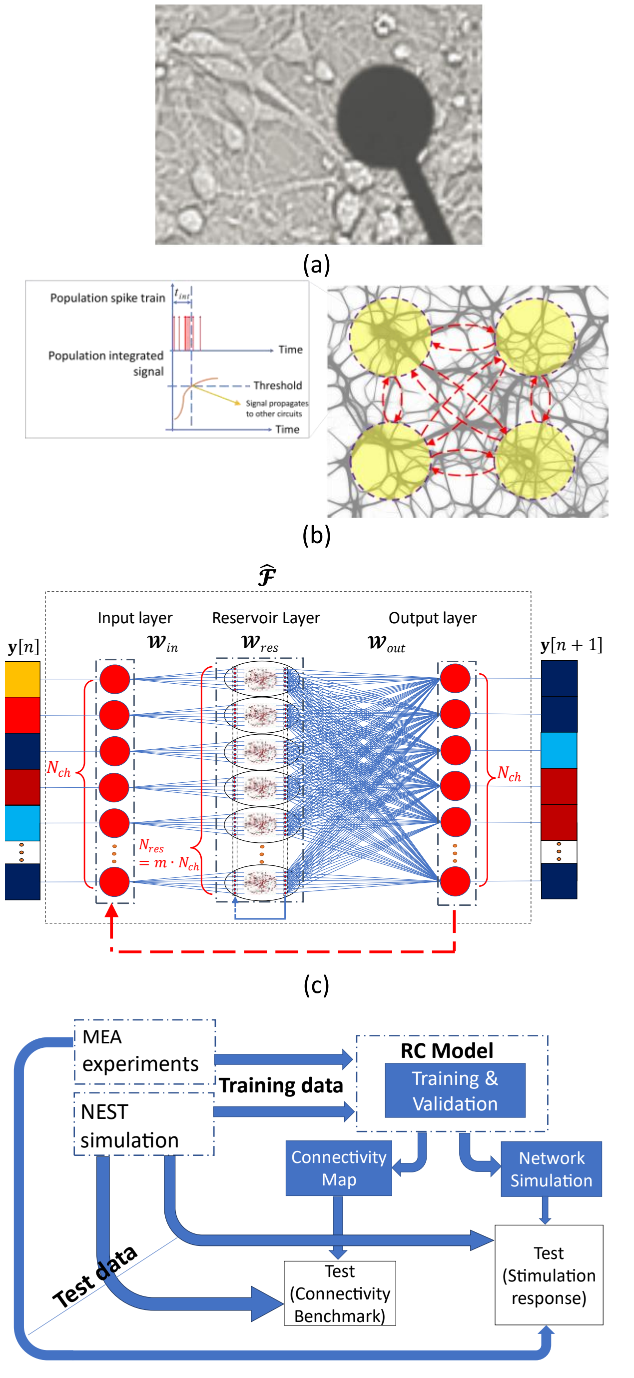

(d)

Figure 16: *Description of the RC model. (a) Microscope image of a microelectrode (diameter of 30 µm) surrounded by cultured neurons. This image illustrates how each electrode samples signals from a complex neuronal circuit. (b) Sketch of how the signals are intercepted by each electrode (yellow circles) from the biological neuronal network in the background. The spike trains collected at each electrode are then forming integrated signals, which propagate within the network. (c) The artificial neural network (ANN) design of the RC model. This consists of three layers (input, reservoir, output) and a recurrent branch. It describes how the state of the network y (described by N_{ch} samples of the measured signals) is processed from time step n to time step n+1. (d) A block diagram of the sequential computational processes.*

In addition, we experimentally demonstrate the ability of the model to predict a network response to a specific input, such as localized stimulus (Fig. 18).

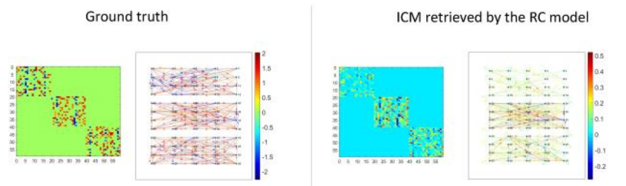

Figure 17: *Connectivity map obtained by the RC model. (a) A connectivity matrix and a connectivity graph map are presented for both the ground truth network (left hand side) and the connectivity map obtained by the RC-model (right hand side). The Ground truth network was simulated on NEST simulator, producing electrophysiological activity, which was then decoded by the RC model. This yields the Intrinsic Connectivity Matrix (ICM). Note that the RC model predicted with a very high accuracy the existence of 3 uncoupled groups. In addition, the model distinguished with a high accuracy between excitatory connections (positive weights) and inhibitory (negative weights). The nodes in the graphs represent neuronal population (or circuit) and the edges represent effective synaptic connections. The predicted map displays only weights with absolute values exceeding 0.1.*

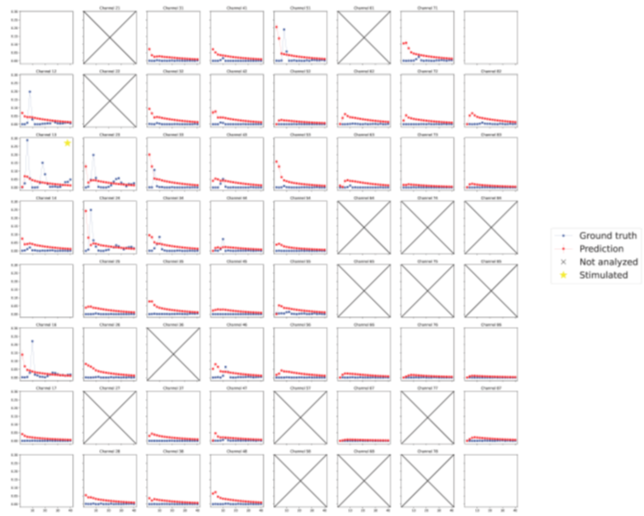

Figure 18: *Map of electrodes response to stimulus given around electrode #13 (designated by a yellow star). Experimental (MEA measurement- blue markers) vs. RC-model prediction (red markers). The y-axis is the normalized instantaneous spike rate (ISR) in arbitrary units as a function of time (x-axis).*

The model's predictions underwent evaluation through a combination of experimental measurements and numerical simulations. Experimental settings involved microelectrode array (MEA) recordings of *in-vitro* mice cortical neurons. Additionally, numerical simulations were conducted using the NEST simulator.

10. Measurement of light induced long-term potentiation in neuronal culture by Multi Electrode Array (Ilya Auslender, Seyedeh Yasaman Heydari)

Here, we explored the creation of a long-term potentiation (LTP) in neuronal cultures using patterned light, and detection by electrophysiological recording. We employed a Microelectrode Array (MEA) system to record the electrical responses triggered by optical stimulation within networks of ChR2-YFP-expressing neurons. The MEA system comprises an array chip housing 60 microelectrodes constructed from titanium-nitride. These microelectrodes are integrated into a transparent glass substrate and enclosed by a surrounding glass ring apparatus, all designed to enable precise monitoring of electrical signals near cultured neurons. In our experimental procedure, the DLP system delivered optical stimulation within a circular area with a diameter of approximately 200 µm (Fig. 19 a). Initially, neurons were exposed to a baseline illumination pattern, featuring 20 ms light pulses at a frequency of 0.5 Hz for a duration of 10 minutes (Fig. 19 b). Then, to induce long-term potentiation (LTP), neurons underwent a stimulation regimen that included 10 sets of 13 light pulses delivered at a frequency of 100 Hz, with a repetition frequency of 0.5 Hz. After the LTP stimulus, neurons were subjected to baseline illumination patterns at four different time points: 0, 20, 40, and 60 min post-stimulation (Fig. 19 c).

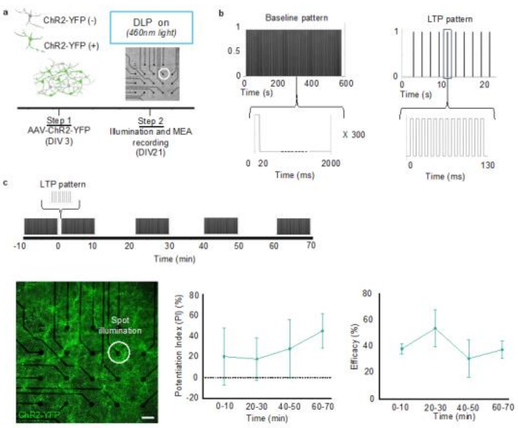

Figure 19: *LTP recording through MEA following light-stimulation. (a) Schematic diagram of the experimental procedures. (b) Schematic representation of the temporal patterns used for baseline and LTP light-stimulation. (c) Timeline representation of the experimental sequence. The image depicts a neuronal network expressing Chr2-YFP grown on a MEA chip. Graphs show the potentiation index and the efficacy at different time points following light stimulation (n=5 experiments). Scale bar: 50 µm.*

To analyze the responses of the neuronal network to light stimulation, we used post-stimulus time histograms (PSTHs) at each electrode. If an electrode exhibited a PSTH with an area under the curve measuring less than '1', it was excluded from the statistical analysis because it was considered inactive. For the active electrodes, the efficacy of potentiation was calculated as the change in the PSTH area between the pre- and post-LTP pattern exposure phases (Fig. 19 c). We established a threshold based on the two baseline recordings to distinguish a potentiated response from spontaneous network activity fluctuations, setting an efficacy threshold of 20%. The Potentiation Index (PI) was subsequently determined as the percentage of the channels that displayed an efficacy higher than the selected threshold at each time step among the active channels, providing valuable insights into the progression of potentiation over time. Our data showed a Potentiation Index above 20%, which increases almost to 50% on average, going from 0 to 60 minutes after the stimulation. The potentiated electrodes show an efficacy of about 40%, which remains almost constant over time (Fig. 19 c).

11. Modelling memory as a meta-reinforced random walk with multiple time-scales (Gianmarco Zanardi)

The brain has always been regarded as one of the most complex network systems in nature, composed of neurons and a multitude of other cells that are collectively referred to as *glia*. A glial cell, named *astrocyte,* is a pivotal component for the long-term persistence of memory which is modelled as an the engram, i.e. a network of neurons preferentially connected. On the theoretical side, multiple valid models of memory formation, retention and retrieval exist, involving various mechanisms of plasticity at different resolutions and complexity in both time and space. However, memory, now to be intended in the broader sense of non-Markovianity, is also an intrinsic or emergent feature in a wide class of other complex network systems, ranging from epidemics spreading to opinion diffusion dynamics on social networks or ecosystem interactions on ecological networks. Our aim is to develop a memory engram model accounting for the role of the glia, showing how it is required for proper memory formation. On the other hand we want also to simplify and abstract the model to make its core dynamics applicable to any network system (in principle).
The model is based on a random walk (RW) process on a recurrent network: it is a very general process, robust enough for statistical considerations yet simple enough to capture an essential picture of memory engram formation and recall. In a RW, the walker chooses a node to reach in each time-step: the probabilities of these nodes to be chosen are proportional to the weights of the edges connecting them to the current node. To introduce memory dynamics, we consider an edge-reinforced RW (ERRW): each time the walker traverses an edge, the corresponding

weight is increased. This edge will then have a higher probability of being traversed again in the future. We pair this with a regularisation function and a decay mechanism. The regulation ensures that the weight growth follows a chosen functional form. Our chosen reinforcement function is a sigmoid function $\boldsymbol{\sigma(s)} = \frac{\boldsymbol{R}}{\mathbf{1+exp(-\kappa s+\xi)}}$, providing the natural benefit of an upper soft bound $\boldsymbol{R}$ to prevent the indefinite growth of weights. The function and the role of its parameters are depicted in Figure . We set $\boldsymbol{R}$ via a relation to another parameter, $\boldsymbol{\mathcal{P}_{max}}$, that controls the asymptotic probability for the walker to choose an infinitely reinforced edge. The decay, on the other hand, introduces a forgetfulness element in the process. The result is a first-order adaptive dynamics that resembles short-term (decay process) memory of Hebbian synaptic strengthening (soft-bounded reinforcement). It is characterised by two independent time-scales: that of memory formation, controlled by parameter $\boldsymbol{\kappa}$ in the sigmoid equation, and that of the decay, expressed by a characteristic time-step $\boldsymbol{\tau}$. Similar dynamics are also used in non-biological networks, e.g. homophily bonding in social interactions.

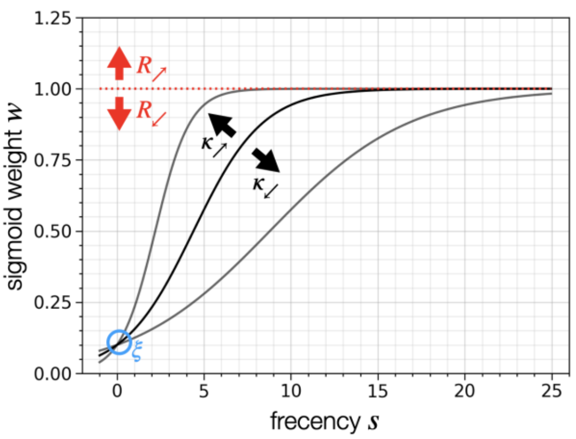

Figure 20: *Exemplary logistic function $\boldsymbol{\sigma(s)}$ (central black curve) for the regularised growth of edge weights and the role of the parameters involved: $\boldsymbol{\xi}$ ensures that in $\boldsymbol{s=0}$ all functions have the same value (see the blue circle); $\boldsymbol{R}$ sets the upper asymptote for the function (see the red dotted line), hence lowering $\boldsymbol{R}$ ($\boldsymbol{R_{\swarrow}}$) shrinks the function and the opposite when it is increased ($\boldsymbol{R_{\nearrow}}$) instead (see the red arrows); finally, $\boldsymbol{\kappa}$ controls how rapidly the function approaches its asymptotes, hence lowering $\boldsymbol{\kappa}$ ($\boldsymbol{\kappa_{\swarrow}}$) flattens the function and the opposite when it is increased $\boldsymbol{\kappa_{\nearrow}}$) instead (see the black arrows and lines). Parameter $\boldsymbol{\kappa}$ sets the time-scale for the reinforcement, i.e. the short-term memory dynamics of our model.*

We then introduce a second component in the dynamics based on the astrocyte-neuron interaction described previously. Because it is neuro-modulative in nature, we implement this as a second-order adaptation that we name *meta-reinforcement*. In practice, parameter $\boldsymbol{\kappa}$ of the reinforcement function becomes time-dependent as $\boldsymbol{\kappa_t} = \boldsymbol{\kappa_0 + \mu}$ where $\boldsymbol{\kappa_0}$ sets the initial time-scale of reinforcement, which we normalise to 1, and $\boldsymbol{\mu}$ is the meta-reinforcement contribution, which grows sigmoidally over its own time-scale and is driven by a Bernoulli stochastic process. Moreover, meta-reinforcement is a locally competitive dynamics: we gather edges in groups of 4, and, for each group, the meta-reinforcement contribution per unit time $\boldsymbol{c^k}$ is split amongst its edges proportionally to their weights. $\boldsymbol{c^k}$, together with the stochastic process probability per unit time $\boldsymbol{p}$, controls the time-scale of meta-reinforcement. Overall, meta-reinforcement resembles a long-term memory that acts on weight growth rates, expressed by $\boldsymbol{\kappa}$, rather than the weights themselves. Equations-wise, our model is suited for any generic recurrent network. Implementation-wise, however, we employed a particular network topology: a cyclic feed-forward network, with nodes organised in layers and each layer being fully connected to the following one with the last connecting back to the first in a cyclic fashion.

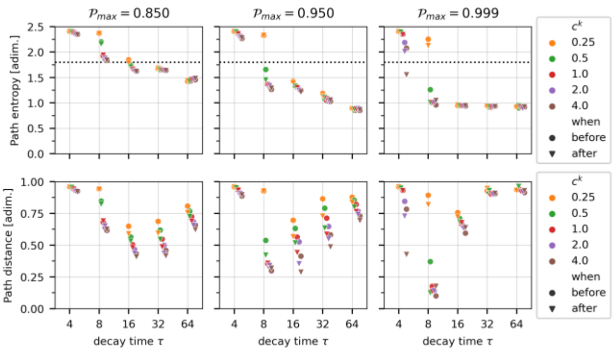

Figure 21: *Path entropy (above) and distance (below) steady state distributions as a function of the decay times (x-axis, in $\boldsymbol{log_2}$ scale), the meta-reinforcement coefficient (colors) for different values of $\boldsymbol{c^k}$. Colors are paired with a slight right-displacement along the x-axis to ease visualization and comparison. Bullet shape reflects when the steady state is computed: before (circular bullets) or after (triangular bullets) edge weights are reset to their initial value to assess the memory recall capabilities of the model. The dotted line in the top panels represents the 1.8 threshold in path entropy that we associate to memorization. Path distance is computed w.r.t. the target path expressed in terms of edge groups*

We simulate the model and test its performances in both memory storage and recall across various parameter combinations. We analyse results in terms of both path entropy and path distance evolutions: the first is a global descriptor of the dynamics, while the second allows a direct comparison between two paths taken by the walker at different times. We try to impose a single closed path of meta-reinforced memory, to assess the capabilities of our dynamics to drive the emergence of a preferred path for the random walker. We compare the behaviour to that of an analogous network deprived of the meta-reinforcement dynamics (we refer to this case as the $\boldsymbol{c^k = 0}$ case in our data). Results show the existence of three regimes, each of which sees one of the three components of the dynamics prevail over the others according to the interplay between their respective time-scales: the decay-dominated regime characterised by the absence of any memory; the reinforcement-dominated regime where uncontrolled short-term memory thrives and meta-reinforcement is not able to impose itself, and the meta-reinforcement-dominated regime where long-term memory thrives due to reinforcement alone not being enough to guide the walker. These results are visualised in Fig. 21 as the steady-state values reached by the system in entropy (above) and distance w.r.t. the imposed path (below): in the decay-dominated regime entropy and distance are both large, in the meta-reinforcement one both are small and in the reinforcement regime entropy remains small while distance grows large again.

This work shows, through a minimal statistical model, the existence of a regime where meta-reinforcement is pivotal for memory formation, as the suppression of it hinders any attempt at memorisation. This is in line with the experimental evidence mentioned above of the fundamental role of an astrocyte-mediated interaction for the long-term persistence of memory. Furthermore, the high degree of generality of our work provides a solid basis to model any network process characterised by multiple memory levels and time-scales.

12. Inducing neuronal hyper excitability in-vitro to model epilepsy using optogenetics tools (Seyedeh Yasaman Heydari)

Epilepsy, a persistent neurological condition, manifests varied symptoms depending on the affected brain region, notably characterized by unpredictable seizures that profoundly affect patients' lives. Here, we aim to establish a robust in vitro model for epilepsy with the vision of leveraging it to advance our understanding and its treatment. Aligned with our objective, we endeavoured to replicate hyperexcitability in primary neuronal cultures. To monitor changes in electrical activity, we utilized Multi-Electrode Arrays (MEA) recordings.

First, we explored the disruption of extracellular ion balance since the Goldman equation emphasizes the role of ion gradients in controlling neuron excitability. Experiments reported that KCL let to transition from burst firing to tonic spike firing or complete cessation of activity due to depolarization-sensitive processes, including the deactivation of voltage-gated channels and neurotransmitter depletion. Our experiments corroborated these findings, where multi-electrode array (MEA) recordings captured the silence of neuronal cultures induced by KCL treatment (Fig. 22).

Then, we explored the effects of Kainic Acid (KA), which is known for its ability to enhance neuronal excitability through targeting glutamatergic receptors. We conducted continuous one-hour recordings using MEA, which revealed a significant increase in spike frequency following KA administration compared to baseline (Fig. 23, left). Control experiments with water did not result in notable changes (Fig. 23, right).

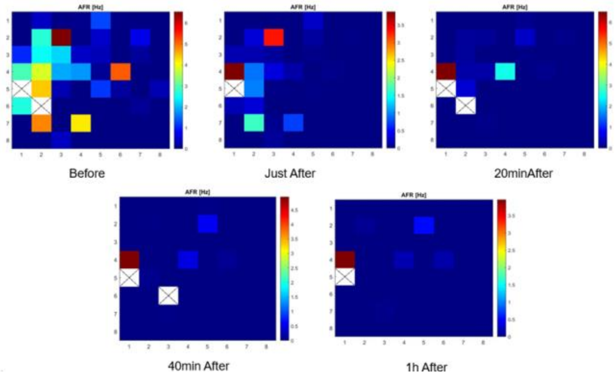

Figure 22: *Electrical Activity of Neuronal Culture in Response to KCl (5mM) over 1 Hour. Different panels refer to different time.*

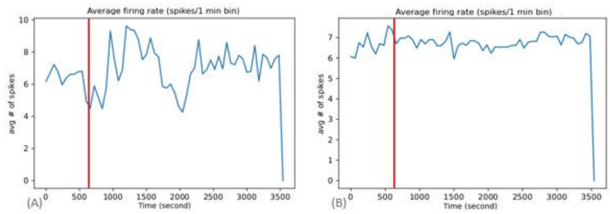

Figure 23: *Continuous one-hour monitoring of neuronal culture electrical activity. Impact of KA (A) and water (B). Recording commenced 10 minutes prior to the introduction of KA (5µM, red lines) and continued for 50 minutes post-administration*

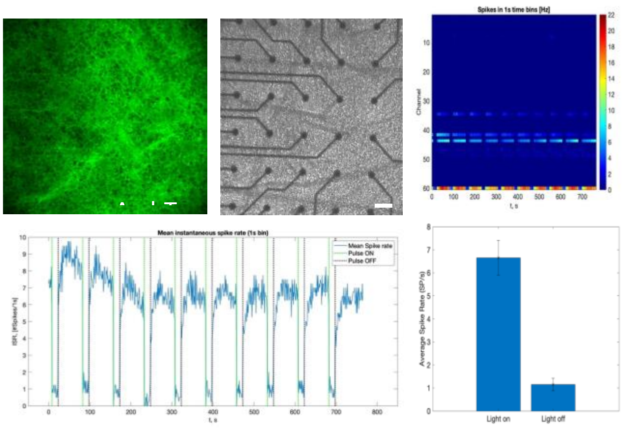

Figure 24: *Performance testing of viral vector pAAV-CamKII-ArchT-GFP in Neuronal Culture. GFP Expression Indicates ArchT Expression (Green Fluorescence), while other figures illustrate changes in electrical activity upon light exposure.*

Finally, we addressed hyperexcitability by an optogenetic tool. We introduced the ArchT channel into neurons through viral vector transduction using pAAV-CamKII-

ArchT-GFP. This viral vector facilitated the expression of Archaerhodopsin (Arch) in neurons. When exposed to 565nm light, Archaerhodopsin pumps out H+ from neurons, thereby inhibiting their activity. By observing the response of the neuronal cultures to these light impulses, we could assess the efficacy and precision of the optogenetic modulation in controlling neuronal activity (Fig. 24).

13. Generation of artificial synaptic engrams for in vitro study (Clara Zaccaria, Asiye Malkoç, Beatrice Vignoli)

Memory is known to reside in specific ensembles of neurons in the brain (*engrams*) whose connectivity encodes for a particular memory. The theoretical basis of memory formation was formulated by Donald Hebb in 1949: "... any two cells or systems of cells that are repeatedly active at the same time will tend to become 'associated' so that activity in one facilitates activity in the other." This 'association' among cells was demonstrated to reside in some permanent modifications, like the reinforcement of their synaptic connections (long-term potentiation and depression, LTP and LTD) and/or the increase in the number of spines among a specific set of neurons during memory trace encoding.

Decoding how specific synaptic ensambles (*synaptic engram*) contribute to the formation of cellular engrams is still largely elusive, and it is difficult to perform these kind of studies in conventional in-vivo experiments. This is where in vitro techniques can offer a controlled environment to examine the mechanisms involved in the operation of the basic circuits involved in memory formation. Here, we validate the Hebb's law in a reliable platform for in-vitro experiments on memory formation. In particular, we used a DLP (digital light projector) system to optogenetically and simultaneously activate 2 neurons in a neuronal network (the simplest concept of engram) and study how their connectivity change, following the stimulus.

To visualize the active synapses in the network and map the connections in an input-specific manner, we used Syn-Active(SA) system. This strategy allows to label the synaptic engram within the global set of synapses, through the expression of HA-tag and Venus, following *Arc* synthesis, an immediate early gene whose synthesis is related to LTP occurrence. We took advantage of tdTomato cellular filler to morphologically localize spines along dendrites (Fig. 25A). After LTP-like illumination of neurons, local *Arc* synthesis can be detected targeting HA with immunocytochemistry techniques, fixing the sample 90 min after illumination, or following Venus appearance in time with live imaging. We thus counted the percentage of HA+ spines along dendrites, morphologically analyzing laser scanning confocal (LSC) z-stack images of illuminated and not illuminated neurons. When 2 neurons in the network are simultaneously excited, an increase of HA+ spines is recorded in illuminated neurons, compared to not illuminated ones, suggesting a potentiation of the connections among the two cells (Fig. 25A).

To confirm this hypothesis, the same experiment was conducted blocking neuronal communication with TTX neurotoxin, or illuminating just 1 neuron in the network (Fig. 25A). The absence of HA+ spines increase in the last two conditions serves as evidence that dendritic spine reinforcement relies on the synchronized activation of two neurons that are being simultaneously excited within a network. This requirement aligns with the principles of Hebb's law. Subsequently, we examined the spatial arrangement of HA+ spines on the pairs of neurons that were stimulated, taking into account the direction of their processes and their respective locations.

Taking as reference the imaginary line connecting the two neurons as 0°, we defined as IN the processes whose direction was in the ±90° range, and as OUT all the others (Fig. 25B). Polar plots of the relative amount of HA+ spines reveal an increase along IN-dendrites, in contrast to the opposite direction (Fig. 25C,D). This suggests a preferred functional connectivity among the engram neurons, again in agreement with Hebb's law.

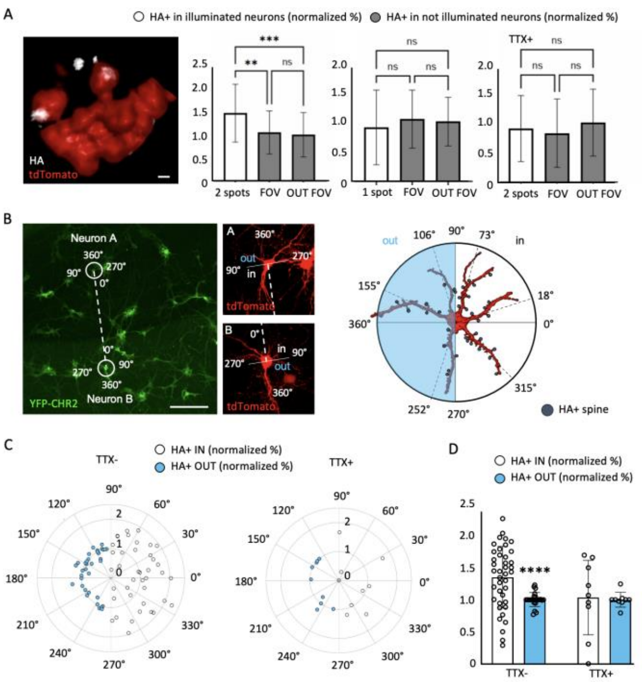

Figure 25: ***A*** *SIM image of two HA+ spines. Scale bar = 1 μm. Bar plots showing the percentage of HA+ spines counted along the processes of illuminated and not illuminated neurons in the field of view (FOV) and out of it (OUT FOV). From left to right are shown the cases of 2 neurons stimulation, 1 neuron stimulation and 2 neurons, in presence of TTX. One-way ANOVA Test.* ***B*** *Sketch showing the categorization of dendrites an IN and OUT. Scale bar = 100 μm.* ***C*** *Polar plots showing the HA+ percentage in IN and OUT processes along the different directions, in presence and absence of TTX.* ***D*** *Average of HA+ percentage in IN and OUT processes in presence and absence of TTX. Unpaired t-test.*

Hence, our system stands as a reliable method for uncovering the dynamic and complex features of synaptic engram circuits. Its value is especially pronounced in situations where live validation is not feasible, establishing it as a crucial tool for grasping the synaptic dynamics within engram circuits. The fundamental simplicity inherent in the binary neuron module, acting as the core building block for more elaborate engram circuits, offers a distinctive viewpoint to investigate the essential rules that orchestrate the formation of functional connections among engram neurons.

14. Exploring memory engram consolidation through optical activation (Paolo Brunelli, Asiye Malkoc, Clara Zaccaria, Beatrice Vignoli, Marco Canossa)

Despite ongoing research, there is no universally accepted model explaining how memories are stored in the brain. Engrams can be categorized into two types: i) active engrams, which can be naturally recalled and utilized, and ii) silent engrams, which cannot be retrieved through natural cues but can be activated artificially. The proposed way to distinguish between these involves the strength of synaptic connections between engram neurons.
According to this theory, active engrams are linked with robust and enduring synaptic connections, while silent engrams are associated to weaker or less stable connections. Brain-derived neurotrophic factor (BDNF) is a pivotal protein in the development and maintenance of neurons, playing a crucial role in synaptic plasticity- the ability of synapses to strengthen or weaken in response to changes in neural activity.

Figure 26: *A cage lid designed for the non-invasive activation of photosensitive molecules in mouse models. This lid features an array of hundreds of LEDs positioned to uniformly illuminate the entire cage with a defined pattern of blue light.*

Astrocytes, non-neuronal cells in the brain, play a crucial role in controlling BDNF availability at synapses. These cells can internalize BDNF secreted by neurons during long-term potentiation (LTP)-inducing electrical stimulation and recycle it in a calcium-dependent manner. The sustained release of BDNF, actively engaging the activation of the TrkB receptor at post-synaptic sites, represents a novel mechanism through which cortical synapses contribute to synaptic changes relevant to memory consolidation. The primary goal of our project is to develop optogenetic strategies for activating TrkB signaling within engram neurons. This approach aims to regulate the formation and consolidation of active memory engrams, potentially restoring impaired memories by manipulating the signaling pathways associated with memory formation.

15. Cellulose-based nanomaterials (Marina Scarpa, Paolo Bettotti, Elvira D'Amato, Arianna Bartolomei, Alessandro Foradori)

Despite being known since centuries, cellulose, particularly its basic constituents at the nanoscale, still reveals innovative properties. United Nations adopted the 2030 Agenda for Sustainable Development that is a document focused on the awareness on the ecological, financial, social, and material sustainability. Urgent actions are required to protect our planet by preserving natural resources and to ensure sustainable consumptions. Such green and sustainable revolution includes electronics. Indeed, growing attention is being devoted to the entire lifecycle of electronics, employing reusable and recyclable materials, thus minimising wastes. Cellulose has significant piezo and triboelectric properties that render it a candidate material to develop self-actuated electronics exploiting energy harvesting strategies.

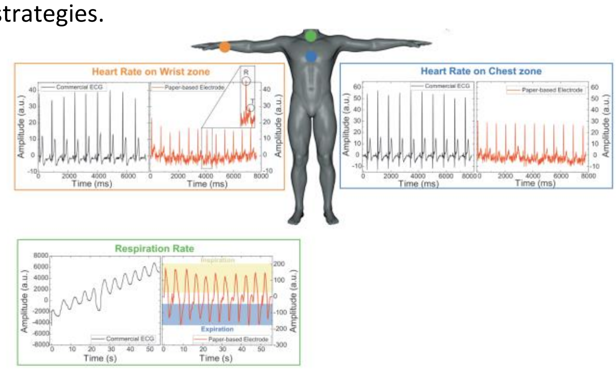

Figure 27. *Three paper-based devices used to monitor heart, wrist and respiration rates. The left (black) signals are registered by commercial health-monitoring devices, while the colored (right) signals are those monitored by the paper-based sensor.*

Within an international collaboration, we demonstrate the possibility to realize electronic devices, such as capacitors, biosensors, and electrodes for food monitoring as well as heart and respiration activity analysis. Moreover, the device is fully recyclable as it is naturally digested in few weeks with no release of harmful compounds. Electronic conductivity is added to the paper by laser carbonizing it.

Another use of Nanocellulose aims to exploit its peculiar properties as membrane for selective gas separation. In particular we demonstrate that they addition of low molecular weight of poly- ethylene glycol (PEG) to self-supporting NC membranes modifies the permeability of gases of relevant environmental and industrial interest, such as CO_2 and H_2 and that the material is selective against CO_2. PEG is a nontoxic and biodegradable polyether compound commonly used as plasticizer for polymers. Given the gas impermeable nature of the NC pure membranes caused by their high packing degree, composite PEG-CNC films permit to tune the transport properties of H_2 and CO_2 and separation performances of the NCs films. This materials combination allows sustainable membrane production considering the low cost, biodegradable nature and pollutant-free production processes of their component, the membrane facile fabrication and feasible upscaling.
Finally, an innovative hybrid hydrogel material made by NC and either alginate or PEG were used as substrates for cell cultures. The in-depth characterization of the material structure allows us to verify the possibility to use commercial Dynamic Light Scattering equipment to check for the dynamic of gelation of the material. In this respect the analysis confirmed that while PEG form a robust gel upon addition of. Mg^{2+}, alginates have a poor affinity with this cation and the gel structure maintain a more liquid structure. Curiously, the macroscopic characteristics sensed with classical rheology do not reveal this difference, as both materials shown similar value of elastic moduli and viscosities. We check the possibility to use these substrates as substrate for cell cultures and they demonstrate a good biocompatibility, in particular, we achieve promising results with co-cultures of neurons and astrocytes on these materials.

16. Marangoni Propulsion of Nanocellulose Gel (Alessandro Foradori, Paolo Bettotti)

Self-propelling objects are items that use the energy from their local environment or carry their fuel to sustain their motion. If they navigate within a fluid, they are known as active swimmers. The propulsion is generated either by a mechanical action or by a chemical phenomenon. In the latter case, a swimmer at the interface between two fluids, e.g. floating on the water surface, must be able to alter the surface tension. The gradient in the surface tension at the water-air interface induces a flow in the liquid, allowing it to move. These objects are named either interfacial swimmers, underlying the importance of the fluid-fluid interface in the origin of their motion, or Marangoni swimmers, after the homonym effect responsible for it.
We studied swimmers made of cellulose hydrogel whose structure traps the surfactant and regulates its release rate. To reveal the underlying mechanics of the Marangoni effect in the motion of a loaded swimmer, several layers of complexity are peeled back. Thus, assuming negligible inertia, the contribution to the speed due to this phenomenon depends on the viscosity in which the object swims, the shape of the object, and the surface tension distribution around it.
A qualitative description of the swimmer's dynamics is provided by relaxing some assumptions about stationarity. When at rest, the swimmer releases surfactant isotropically into the pool, which diffuses and creates a gradient in surfactant concentration, inducing a Marangoni flow. This flow, in turn, moves the surfactant around (advection). If the advection is sufficiently larger than the diffusion, the symmetry is broken and the start of the swimmer motion is allowed. The motion itself favors a front-back asymmetric distribution of the surfactant concentration. This feedback modulates the speed of the object that, depending on the level of turbulence its motion creates, might propel under very different and peculiar dynamics.
Due to the macroscopic scale of the system, the motion of the swimmers occurs in a turbulent regime. In such a scenario, numerous approximations of the theoretical models fail, necessitating the adoption of a phenomenological approach to unveil the role of the main parameters on swimmer motility.

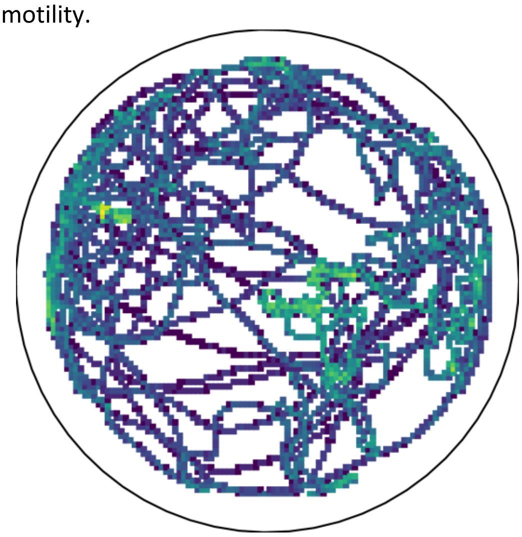

Figure 28: *Example trajectory: positions of a circular swimmer for viscosity 45.8 mm^2s^{-1}. The color scale represents the logarithm of the probability density function, where the minimum value greater than zero is represented in purple, while the maximum one is bright green and the black contour is the 112 mm internal pool diameter.*

Nanocellulose hydrogel has emerged as a noteworthy development, displaying its capacity to act as a robust frame that can be permeated by solvents via diffusion. We are pioneering the exploitation of this material to construct surfactant-loaded Marangoni swimmers. We opt for alcohols with distinct carbon chain lengths as fuel sources. A careful characterization of the alcohol gels reveals the composition of the loaded solution, including solvent proportions, and air and water content. Regarding the propulsion dynamics, the motion of a swimmer in a pool is tracked with a camera. Figure 28 illustrates an exemplary trajectory, while Fig. 29 shows a representative speed profile; both figures highlight the complicated motion of the system. The experiments aim to shed light on the intricate interplay between composition, shape, liquid viscosity and propellant surface tension of the swimmer and demonstrate the possibility of obtaining a (semi) quantitative estimation of the energy contained within the swimmers by looking at their trajectory.

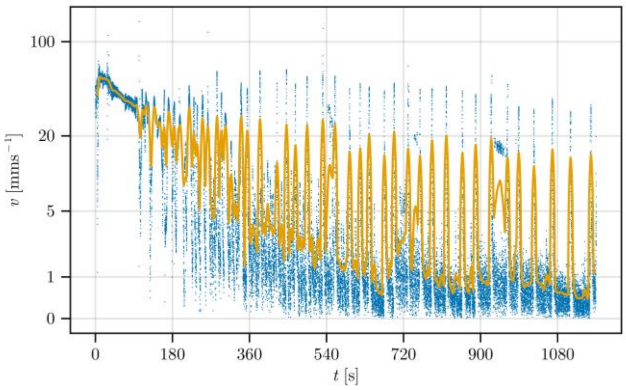

Figure 29: *Example trajectory: velocities of a circular swimmer for viscosity 3.83 mm^{2}s^{-1}. The blue dots represent the measured data, while the yellow line is a triangular moving average of them.*

17. Developments in integrated quantum photonic circuits at near-visible wavelengths (Matteo Sanna, Alessio Baldazzi, Nicolò Broseghini, Stefano Azzini)

Quantum simulators represent advanced quantum systems designed to solve quantum problems in fields such as biology, chemistry, and solid-state physics. They provide a powerful solution to computational challenges that exceed the capabilities of classical computers. Quantum applications do not inherently favor a specific material platform, as each one of them has its strengths and weaknesses. Integrated quantum photonics emerges as a promising platform for building quantum simulators, offering the advantage of simplified manipulation and precise control of photons.

Our current efforts involve the development of a silicon nitride (SiN) photonic platform operating in the visible-to-near-infrared (VIS-NIR) spectral region. This platform aims to integrate single-photon avalanche diode (SPAD) detectors into silicon to create a quantum simulation (QS) photonic device operating at room temperature and integrating, with a 3D approach, the control electronics as well. This is the final goal of the European project EPIQUS (Electronic-Photonic Integrated Platform for Quantum Simulations), led by the Bruno Kessler Foundation in Trento (FBK). Investigations were conducted on the integrated linear structures, which are essential for the implementation of the simulator. The main devices include crossing waveguides, multimode-interferometer-based integrated beam splitters (MMIs), microring resonators, as well as symmetric (MZIs) and asymmetric (aMZIs) integrated Mach-Zehnder interferometers based on MMIs. The MMIs are designed and tested in two different configurations. If the interference mechanism involves all modes, the structure is referred to as general interference MMI (G-MMI). On the other hand, if the input waveguides are positioned to couple to only some modes of the multi-mode waveguide, a different interference scheme is obtained. Specifically, in this case, we design the MMI to achieve mode-pair interference only and refer to it as P-MMI. Another important structure under consideration is the aMZI. The aMZIs are crucial for the realization of an integrated filter for residual pump beam removal on-chip. Implementing a cascade of 4 aMZIs, a rejection value of 64 dB was measured without active control. Further details are given in Table 1.

The quantum light used in this platform is generated by a microring resonator source that is based on a nondegenerate spontaneous four-wave mixing (SFWM) process, a third-order nonlinear optical interaction in which two pump photons scatter into one signal and one idler photon at different energies, symmetric with respect to the pump.

Structures	ILs	main feature
Crossing	0.15 dB	Modal cross talk< -60 dB
G-MMI	<0.5	Unbalanced: 0.2 dB
P-MMI	<0.5	Unbalanced: 0.7 dB
Integrated Filter	2.1 dB	Rejection: 64 dB

Table 1: *Main features of our SiN integrated structures measured in TE polarization around 740 nm.*

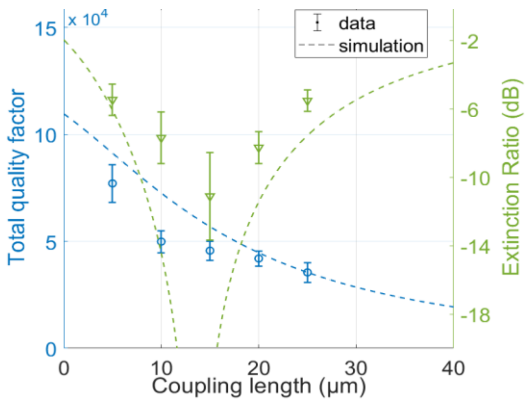

Figure 30: *Total Q-factor (light blue) and Extinction ratio (green) as a function of the coupling length around the wavelength of 800 nm. Points represent experimental data. Dashed lines show the simulation results.*

Our microring resonators have been designed and fabricated with a racetrack configuration featuring a radius of 30 μm. Figure 30 illustrates the dependence of the Q factor (light blue dots) and extinction ratio (ER, green dots) on the coupling length (Lc) around the working wavelength of 800

nm. Additionally, the graph includes FDTD simulations results represented by dashed lines. Notably, a nearly critical coupling regime is observed at Lc= 15.0 µm, where the measured values of Q_{crit} = (4. 5± 0.2)x10^4 and ER= (-11 ± 3) dB align fairly well with our simulations.
In SFWM, signal and idler photons of the same pair are emitted at the same time. Preliminary measurements of the coincidence-to-accidental ratio (CAR) of the nonlinearly generated photon pairs are performed at 780 nm. The measured CAR values assess the effectiveness of signal-idler pairs generation in our setup. So far, our maximum measured CAR value is 2.45 at 8.3 mW on-chp power, in line with the state of the art in this spectral region.

18. Toward a variational quantum eigensolver circuit on a silicon chip (Leonardo Cattarin, Matteo Sanna, Alessio Baldazzi, Stefano Azzini)

Quantum chemistry requires the analysis of complex molecules, whose energy structures helps understanding their chemical dynamics for applications in pharmaceutical design and materials science. Variational quantum eigensolver (VQE) is a hybrid variational method able to calculate the ground state of chemical systems. The algorithm relies on the encoding of the molecule's states in the physical qubits of the quantum hardware and on the ability to map the molecular Hamiltonian in terms of elementary operations on the qubits, given by Pauli strings. The quantum hardware is designed to allow the preparation of parameterized generic trial quantum states. A classical processor (CPU) is, then, used to control the quantum hardware parameters, allowing the exploration of the states' configuration space. From the measurements, we collect the statistics to obtain the expectation value of the Pauli strings that constitute the translated Hamiltonian. Then, the CPU uses these quantities to evaluate the expectation value of the full Hamiltonian on a given prepared trial state. Depending on this result, the CPU updates the setting of the quantum hardware, and the cycle is repeated until the minimization of the energy expectation value is achieved. The VQE converts the computational problem into a sampling problem, where the CPU manages the operations and the raw data provided by the quantum part.
In our case, the VQE algorithm has been translated into an integrated circuit in silicon photonics. A photonic chip (Fig. 31) composed of integrated heralded single-photon sources and manipulation stages has been designed. Then, an external foundry through a commercial service fabricated the device. The integrated sources are four spiral waveguides that exploit Spontaneous Four-Wave-Mixing (SFWM) to generate a superposition of one pair of non-degenerate photons around 1550 nm propagating among four paths. This choice fixes the dimension of the configuration space to four qubits. The manipulation part is used to separate the generated twin photons and route them to Mach-Zehnder interferometer (MZI) networks that implement the Pauli strings action.

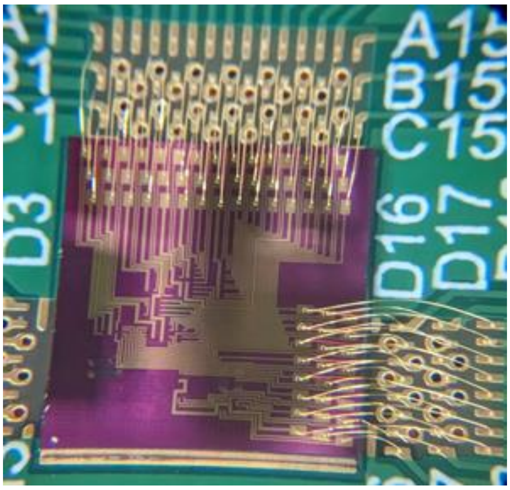

Figure 31: *Integrated silicon chip that contains the VQE circuit. The chip has metal parts connected to a PCB by gold wires.*

From an experimental point of view, the chip will be tested in a newly developed set-up. The fact that the most delicate measurement stages are either integrated or fiber-coupled will ensure a good overall stability of the experimental setup, for which a remote control will be available. At the time of writing, a characterization of the integrated MZIs and of the SFWM-based spiral waveguides sources present in the circuit is ongoing.

19. A linear photonic swap test circuit for quantum machine learning (Alessio Baldazzi, Nicolò Leone, Matteo Sanna, Stefano Azzini)

One of the most robust and efficient supervised learning models in machine learning is the vector-support machine (SVM), which is used to classify clusters of data. Such a method can discriminate the elements of a dataset based on their properties and assign them to a predetermined category.
Such a classification task is based on the representation of each data in a feature space: the data set's properties span the feature space along the axes, and each element is identified as a point in such space. In this representation, the classification is achieved by identifying hyperplanes that separate the various categories. The task is quite simple if we consider linearly separable sets. However, when a set is not linearly separable the classification procedure is not straightforward. This issue can be overcome by selecting other properties to enlarge the feature space in the so-called implicit feature space. The effect of the extra properties is encoded in a kernel function, which gives the euclidean distance between data in the original feature space. Noteworthy, kernel functions can always be written as scalar products. This feature has suggested the creation of classical-quantum hybrid approaches that involve the

use of quantum hardware, since quantum mechanics offers a natural framework to calculate scalar products. The main purpose of the quantum part relies on the promised speed-up in the computation of the scalar products needed to define the data distances for the classification.

The SWAP-test is an example of a quantum algorithm that can be implemented in a hybrid fashion to calculate the scalar product of two generic quantum states $|\psi\rangle$ and $|\xi\rangle$. By encoding the data in quantum states prepared in the quantum hardware, such an algorithm gives as a result the entries of the kernel function by measuring the outcomes of an ancillary qubit initially prepared in the $|0\rangle$ state. At the hearth of the swap test there is a controlled-swap gate (CSWAP) applied to the state, whose action is to swap the two other states when the auxiliary qubit is in $|1\rangle$ state. After applying the swap test on the state $|\psi\xi 0\rangle$, the expectation value of the measurement operation on the ancillary qubit $|x\rangle$ is given by $P(x) = 1/2(1-(-1)^x\,|\langle\psi|\xi\rangle|^2)$.

Thus, it is possible to translate the scalar product calculation into a sampling problem: we need to acquire statistics in order to evaluate the kernel function entries. The quantum advantage relies on the scaling of data encoding and of the sampling procedure with respect to the number of data. We have decided to implement the swap test algorithm on an integrated photonic chip: the qubits are encoded in the path of the photons and the manipulation is achieved by integrated Mach-Zehnder interferometers. In particular, the CSWAP operation has been implemented using only linear optical integrated components, thanks to the exploitation of path-encoded single photon states. This choice simplifies consistently the structure of the photonic circuit, since we do not have to rely on probabilistic two-qubits gates that would lower its performances.

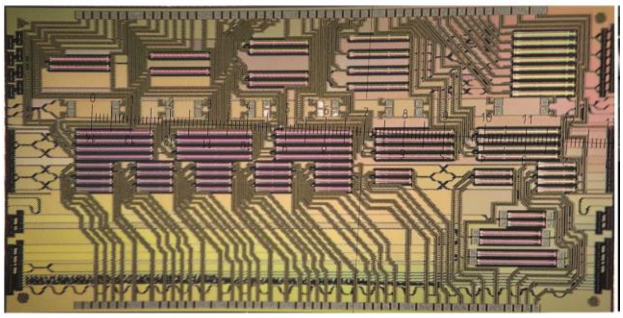

Figure 32: *An optical photo of the SiN photonic chip containing the swap test circuit.*

Figure 32 show a photo of the silicon nitride (SiN) integrated chip, which contains the swap test photonic circuit, while Fig. 33 show the result of on experiment, in which fifty couples of random states $|\psi\xi\rangle$ are encoded and injected in the swap test circuit. As we can see, the results match the theoretical prediction, with only slight visible deviations. These deviations are primarily due to the realistic characteristics of the PIC, such as the non-ideal performance of some photonic components. In the figure, the red intervals represent such behavior, and the majority of the experimental data falls within these intervals.

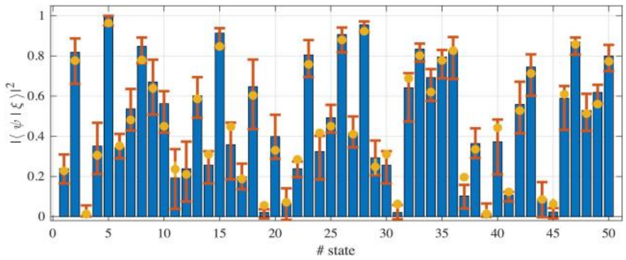

Figure 33: *Results of the swap test experiment. In blue, the theoretical expectation value of the scalar product; in yellow, the experimental data obtained, while in red a confidence interval taking into account the circuit non-idealities.*

20. Programmable silicon photonic chips for high-purity and indistinguishable photonic qubits (Alessio Baldazzi, Matteo Sanna, Stefano Azzini)

The collaboration with JM Lee at ETRI, South Korea, produced new results on the indistinguishability of photon pairs sources. Experiments on spiral waveguides and microring resonators enables the comparison of these two types of integrated photon-pair sources utilizing Hong-Ou-Mandel (HOM) interference. We carried out a theoretical analysis showing that the visibility of the HOM pattern is dependent only on the overlap of the Joint Spectral Amplitudes (JSA) of a pair of sources, which quantifies their indistinguishability. This is because the two sources are coherently pumped and produce a path-entangled state for two pairs of photons. Experimentally, we observed that the visibility and consequently the JSA overlap of spiral waveguides is higher than the ones of microring resonators. In particular, spiral waveguides showed a value for JSAs overlap of 98% and microring resonators 89%. Simulating the effect of imperfections due to the fabrication process, we showed that the overlap of the JSA is more sensitive in the case of the microring resonators with respect to the spiral waveguides. The main results for the study of the JSA overlap are shown in Fig. 34.

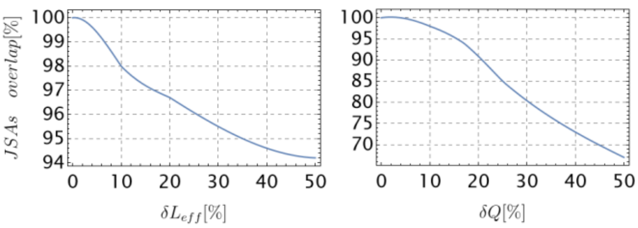

Figure 34: *Simulation of JSA overlap of two spiral waveguides with different effective lengths (left) and two microring resonators with different quality factors Q (right).*

In the simulations, we are considering the case of two spiral waveguides with different effective lengths (Fig. 34 left), i.e. a combination of length and propagation losses, and two microring resonators with different quality factors (Fig. 34 right). The conclusion is clear: even if the microring resonators are characterized by higher generation probability and more efficient filtering of the residual pump, spiral waveguides have a higher performance in terms of indistinguishability. Indeed, to obtain a reduction of JSA overlap comparable to that of microrings, a huge variation in effective interaction length is needed. Therefore, in applications where more sources with a high degree of indistinguishability are required, spiral waveguides are more suitable than microring to implement an integrated pair source.
These results represented the starting point for further advancements and studies in our collaboration with ETRI. Indeed, as a successive step, a circuit composed of four waveguide-based sources has been implemented to exploit non-degenerate SFWM and different stages of manipulation achieved by MZIs. First of all, we measured HOM interference with an impressive result from a pair of heralded photons. This result is not only dependent on the high level of indistinguishability, but also on the purity of the produced photon states. Using two different bandwidth detection filters, the visibility of the pattern is 90% and 98%, respectively, which is compatible with the simulations that we performed. Then, the integrated photonic circuit made it possible to test different configurations: a heralded single qubit, a Bell state, a 4-qubit system with two simultaneous Bell states, and a 4-qubit Greenberger–Horne–Zeilinger (GHZ) state. Each of these cases exhibits a high value of fidelity and purity. Additionally, the entanglement of the 4-photon GHZ state has been verified through Bell's inequality violations and a negative entanglement witness. All these configurations are obtained by tuning thermal phase shifters in order to obtain the desired entangling gate in the integrated circuit.

21. Measurements with undetected photons on a silicon integrated circuit (Chiara Michelini)

The undetected photon technique manages to surpass classical limitations in measurement sensitivity by employing pairs of entangled photons. In a measurement with undetected photons, one photon (the signal) interacts with an object, and the properties of the object can be retrieved by measuring only its entangled counterpart (the idler). By using intermodal SFWM, the entangled photons can be generated at different wavelengths so that the signal photons are in a spectral region suitable for the interaction with the object of interest, while the idler photons are in a spectral region where the detection is efficient. The signal photons are discarded (undetected), and the information regarding the object is obtained by detecting the idler photons, which did not interact with the object.
Up to now, undetected photon measurements have been carried out in bulk configurations only.
In collaboration with ICFO - Institut de Ciències Fotòniques in Spain, we performed undetected photon measurements on a silicon-on-insulator integrated circuit. Our integrated sources generate pairs of entangled photons in the mid-infrared (MIR) and the near-infrared (NIR) spectral regions when pumped with a coherent beam in the C-band. The MIR is a spectral region functional for imaging and spectroscopy since many molecules have strong absorption lines in the MIR. However, MIR detectors are less efficient and exhibit a lower signal-to-noise ratio than detectors sensitive to the NIR spectral region. For this reason, MIR-NIR entangled photon pairs are a suitable choice for gas sensing by the undetected photon technique. As a proof-of-principle experiment, we applied a phase shift to the MIR photon, and we were able to retrieve such phase by only measuring the NIR photon and monitoring the phase applied to the pump beam (Fig. 35). Phases are applied by means of thermo-optic phase shifters using metallic heaters.

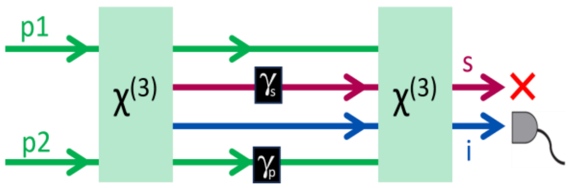

Figure 35: *Scheme of the experiment. Two χ(3) nonlinear sources made of silicon are coherently pumped with two classical beams (p1 and p2). Two pairs of photons, idler (i) and signal (s) are generated via intermodal spontaneous four-wave mixing. The pump beams are in the transverse electric (TE) polarization, in the fundamental (TE0) and in the first excited (TE1) optical mode, at wavelength 1568 nm. The idler photons are generated in the TE0 optical mode at wavelength 1291 nm, while the signal photons are in the TE1 optical mode, at wavelength 2 µm. The paths of the generated photons are superposed and the sources are identical. Between the two sources, we apply a phase shift ɣs to the signal and a phase shift ɣp to one of the pump beams. The phase shifts are applied with an electrical control that exploits the Joule effect. Only counts from idler photon detection are considered.*

Scanning the phase ɣp of the pump beam, the probability amplitude of generating photons in the first source interferes with the probability amplitude of generating the photons in the second source. Consequently, we observe an interference pattern in the idler photon counts. In addition, due to the entanglement between the idler and the signal photons, the probability amplitudes interfere when applying a phase shift to the signal photon since the phase ɣs is carried by the whole entangled state. This can be observed by looking only to the idler photon counts.

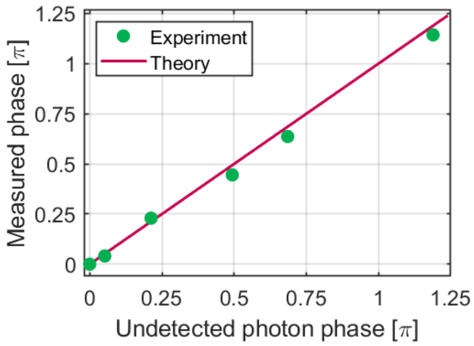

Figure 36: *X-axis: phase ɣs applied to the MIR photons. Y-axis: phase shift in the interference patterns obtained by detecting the NIR photons, corrected by a cross-talk phase contribution carried by the pump used for generating the entangled photon pairs in the second nonlinear source. Dots: Experimental data. Solid line: expected result.*

Acquiring different interference measurements by scanning ɣp for different values of ɣs, we observe that the interference patterns are shifted relative to each other by ɣs. In this way we can retrieve the applied signal photon phase shift by measuring the idler photons. The experimental results are shown in Fig. 36, where a 1-to-1 correspondence between the measured phase and the applied phase is observed. Our results prove that it is possible to perform undetected photon measurements by using an optical integrated circuit, with the advantages of smaller size, less cost, and alignment stability compared to bulk setups.

22. Single-photon entanglement for QKD: proof-of-principle experiments (Nicolò Leone, Alessandro Zecchetto, Stefano Azzini)

Entanglement is one of the most valuable resources offered by quantum mechanics, which has been studied and applied in various fields, from communications to computation to sensing. In quantum communications in particular, previous works have proposed and experimentally proved that entanglement can be used to achieve more secure protocols of quantum key distribution. The latter is a fundamental quantum cryptography tool used by two users, usually called Alice and Bob, to create and exchange a cryptographic key between them. Traditional QKD protocols usually do not exploit entanglement and, even though considered secure, are vulnerable to a higher number of quantum attacks than entanglement-based QKD protocols. However, entanglement protocols are usually technologically more demanding and not easily deployable due to a larger complexity of setups, and to the fragility of entanglement itself.
Single-photon entanglement (SPE) is a peculiar type of entanglement in which two degrees of freedom (DoFs) of a photon are entangled. Compared to inter-particle entanglement between two photons, SPE requires only linear optical components as beam splitters and polarization rotators. In addition, no high power pump sources are involved as in parametric entangled photon sources, suchas those based on Spontaneous Parametric Down Conversion and Four Wave Mixing. SPE represents a promising trade-off between the feasibility of implementation and the security of the protocol since it can be generated more easily and enables QKD protocols that are more secure with respect to faulty or malicious devices.
We have realized a bulky optical setup to test and validate a QKD protocol with SPE states. In the experimental setup, the entanglement between the polarization state of the photon and the direction of propagation of the photon has been used, employing the same methodology demonstrated in our previous work. Photons are generated by an attenuated green laser beam. The setup consists of three main stages: the preparation stage, Alice's station, the transmission stage where the photon is sent from Alice to Bob, and the detection stage at Bob's station.

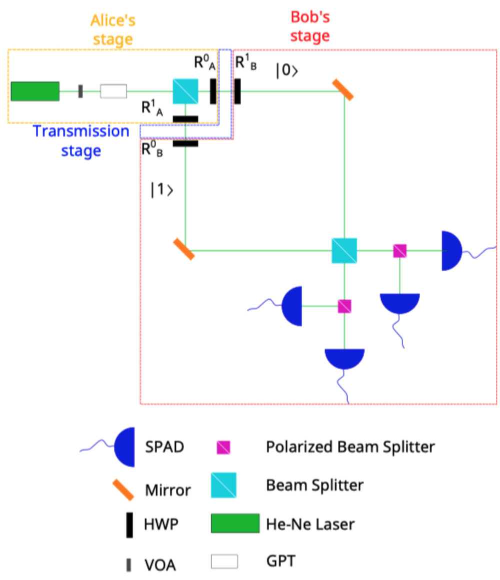

Figure 37: *Experimental setup for the verification of the SPE-based QKD protocol. SPAD: single-photon avalanche diode, HWP: half-wave plate, VOA: variable optical attenuator.*

This is illustrated in Fig. 37. Alice's station is composed by the attenuated green laser, a beam splitter and two half-wave plates (HWPs) used to prepare the state. Bob's station is instead composed of two HWPs, two polarization beam splitters (PBS) and four single-photon avalanche diodes (SPADs). In particular, Alice and Bob, before the start of the protocol, agreed on a particular set of unbiased bases that has to be used. Then Alice, randomly selects one of those bases and prepares randomly one of the SPE states by suitably rotating her HWPs. Then, the state is sent to Bob, who randomly chooses one of the bases and performs the measurement operation on the state, by rotating his HWPs, and projecting the state on the computational basis, with the help of the PBS and the SPADs. If Alice and Bob have chosen the same basis, the result of the measurement operation is deterministic, otherwise it is probabilistic. The cryptographic key is then reconstructed through the deterministic cases, while the security analysis is done on the probabilistic ones. In particular, if the error rate of the transmission exceeds a certain threshold, Alice and Bob can conclude that some problem occurred during the transmission and they discard the key. Otherwise, the generated key can be safely used.

In our experiment, we have preliminarily validated the protocol by observing if the results of Bob's measurements given the state sent by Alice are in agreement with a quantum mechanical description. Then, we sent multiple states from Alice station to Bob's one, which measures the state on a chosen basis.

In particular, for the deterministic result, we obtain that the results of Alice and Bob are in accordance with a probability higher than 90%. This is a piece of evidence that the protocol works as expected. In the other case, the results of Bob are probabilistic. To validate the protocol's robustness, further steps have to be undertaken, like introducing real quantum attacks. Moreover, we are currently working on integrating the bulk setup into two photonic chips, which will serve as Alice's and Bob's stations. These stations will be connected via optical fibers, and the momentum and polarization DoFs will be replaced with more suitable degrees of freedom.

For more info:

Nanoscience Laboratory
Department of Physics
University of Trento
via Sommarive 14
38123 Povo- Trento (Italy)
http://nanolab.physics.unitn.it/

Laboratory assistants
Dr. Chiara Rindone
email chiara.rindone@unitn.it
Dr. Camilla Kandamulla Arachchige
Email c.kandamulla@unitn.it
phone +39 0461 283172